

4-1-1994

Characterization of the radiometric performance of an IR scene projector

Gary Ralph

Follow this and additional works at: <http://scholarworks.rit.edu/theses>

Recommended Citation

Ralph, Gary, "Characterization of the radiometric performance of an IR scene projector" (1994). Thesis. Rochester Institute of Technology. Accessed from

This Thesis is brought to you for free and open access by the Thesis/Dissertation Collections at RIT Scholar Works. It has been accepted for inclusion in Theses by an authorized administrator of RIT Scholar Works. For more information, please contact ritscholarworks@rit.edu.

CHARACTERIZATION
OF THE RADIOMETRIC
PERFORMANCE OF AN IR SCENE PROJECTOR

by

Gary M. Ralph

B.E.E. Royal Military College

(1988)

A thesis submitted in partial fulfillment of
the requirements for the degree of
Master of Science in the
Center for Imaging Science in the
College of Imaging Arts and Sciences
of the Rochester Institute of Technology

April 1994

Signature of the Author Gary M. Ralph

Accepted by June 2, 1994

COLLEGE OF IMAGING ARTS AND SCIENCES
ROCHESTER INSTITUTE OF TECHNOLOGY
ROCHESTER, NEW YORK

CERTIFICATE OF APPROVAL

M.S. DEGREE THESIS

The M.S. Degree Thesis of Gary M. Ralph
has been examined and approved by the
thesis committee as satisfactory for the
thesis requirement for the
Master of Science degree

Dr. J. Schott Thesis Advisor

Dr. R. Easton

Mr. C. Salvaggio

6/2/94
Date

THESIS RELEASE PERMISSION FORM
ROCHESTER INSTITUTE OF TECHNOLOGY
COLLEGE OF IMAGING ARTS AND SCIENCES

Characterization of the Radiometric
Performance of an IR Scene Projector

I, Gary M. Ralph, hereby grant permission to the Wallace Memorial Library of R.I.T. to reproduce my thesis in whole or in part. Any reproduction will not be for commercial use or profit.

Date 10 APRIL 1994

Signature _____

ABSTRACT

A quantitative evaluation of a self-emitting far IR scene simulator is performed. The simulation system is comprised of a white-light source, spatial light modulator, optics, and a visible-to-infrared transducer. The performance was evaluated by measuring the MTFs of the system and subcomponents and the thermal contrast. An attempt to correct variations in the radiometric response across the scene is done by modifying pixel values. Additionally, the effect of cooling the infrared transducer on the thermal contrast is investigated. Results are compared to a previous system which used a coherent light source.

ACKNOWLEDGEMENTS

I wish to acknowledge Dr. J. Schott and Dr. R. Easton for their help and guidance throughout my thesis. Ms. S. Chan and Ms. C. Kitchen for their administrative help which made life at CIS easier. Mr. T. Gallagher for his handling of the many minor crises throughout this project and especially for his technical expertise and many weeks of assistance. Rick Akers, Naoya Katoh, Rich Stark, Brian Backer, Marc Comeau, Tom Haake, Joe Chapa, and Bill Kinder for their assistance and friendship.

INDEX

	<u>Page</u>
List of Figures	viii
SECTION 1 - Introduction	1
SECTION 2 - Background Information	3
2.1 Thermal Imaging System Background	3
2.2 Far-IR Characteristics	3
2.3 Far-IR Imaging Systems	7
2.4 Far-IR Simulation	9
2.5 Ambient Temperature effects	15
2.6 Radiometry	19
2.7 Optical Transfer Function	30
SECTION 3 - Far IR Simulation Design	38
3.1 Energy Source	39
3.2 Spatial Light Modulator	39
3.3 Optics	44
3.4 Visible-to-IR Transducer	44
3.5 Viewing System	46
3.6 Radiometric Normalization	47
3.7 Cooling system	48
SECTION 4- Experimental Methods	50
4.1 System Setup and Alignment	51
4.2 Modulation Transfer Function	51
4.3 Inframetrics Viewing System	54
4.4 MTF of Simulation System	54

4.5 Measurement of Noise-Equivalent Temperature Change	56
4.6 Measurement Procedures	56
5.0 Results	59
5.1 Spatial Light Modulator	59
5.2 Viewing System	72
5.3 Bly Cell	73
5.4 System Performance	73
6.0 Conclusions and Recommendations	76
References	81
Appendix A - Spatial Light Modulator	
Appendix B - VIRT Specifications	
Appendix C - Inframetrics Specifications	
Appendix D - Computer Programs/Routines	
Appendix E - MathCad routines for MTF	

List of Figures

Figure 2-1	Spectral distribution of blackbodies	5
Figure 2-2	A simplified detector	9
Figure 2-3	Ambient temperature differentials	18
Figure 2-4	Solid angle	20
Figure 2-5	Intensity	22
Figure 2-6	Exitance	23
Figure 2-7	Radiance	24
Figure 2-8	Irradiance	25
Figure 2-9	Flux collected by a lens	27
Figure 2-10	System components affecting radiometry	29
Figure 2-11	Perfect lens MTF	32
Figure 2-12	Formation of an edge trace	36
Figure 3-1	Block diagram	38
Figure 3-2	Nematic crystal	42
Figure 3-3	VIRT construction	46
Figure 4-1	System Setup	50
Figure 4-2	Inframetrics viewing system test setup	54
Figure 5-1	SLM image	59
Figure 5-2	Vertical LCD pixels	60
Figure 5-3	Vertical MTF of LCD	60
Figure 5-4	Horizontal LCD pixels	61
Figure 5-5	Horizontal MTF of LCD	61
Figure 5-6	Horizontal pixels for Inframetrics	63
Figure 5-7	Horizontal MTF of Inframetrics	63
Figure 5-8	Vertical pixels for Inframetrics	64
Figure 5-9	Vertical MTF for Inframetrics	64
Figure 5-10	Horizontal pixels of Bly cell	65
Figure 5-11	Horizontal MTF of Bly cell	65
Figure 5-12	Vertical pixels of Bly cell	66
Figure 5-13	Vertical MTF of Bly cell	66
Figure 5-14	Horizontal pixels from system	67
Figure 5-15	Horizontal MTF of system	67

Figure 5-16	Vertical pixels of system	68
Figure 5-17	Vertical MTF of system	68
Figure 5-18	IR image of "E"	69
Figure 5-19	Image of flat field as input	69
Figure 5-20	Image of corrected flat field input	70
Figure 5-21	Image of corrected flat field image	70
Figure 5-22	Image of test image	71
Figure 5-23	System image of 5-22	71
Figure 5-24	Calibration of Inframetrics Camera	72
Figure 5-25	Effect of temperature on contrast	75

1.0 Introduction

The human eye can see electromagnetic radiation in the range of wavelengths between 0.4 and 0.7 μm , which is called the visible spectrum. However, additional information can be obtained about objects from the electromagnetic spectrum outside of this range. Ultraviolet, X-ray, and Gamma radiation are found at wavelengths shorter than the lower limit of the visible spectrum. Infrared radiation, microwaves, and radio waves are at wavelengths longer than the upper limit. The infrared (IR) region is generally accepted to extend from .7 to 14 μm , and is commonly split into smaller subregions: the near-IR (0.7-1.3 μm), mid-IR (3-5 μm), and far-IR (8-14 μm).

Far-IR imaging converts the IR radiation from energy in the $8 \leq \lambda \leq 14 \mu\text{m}$ range into a visible image. Because it measures emitted rather than reflected radiation, far-IR imaging allows day and night operation and covert sensing. The uses of far-IR imaging are wide ranging and include civil, industrial, medical, scientific, and military applications (Burnay, 1988).

Far-IR systems require testing during the development stage and sometimes require periodic calibration. A system to generate far-IR images is required to test complete systems. Several technologies have been developed for

simulating a far-IR scene with varying degrees of success. The work presented here describes a laboratory system that is an attempt to simulate far-IR scenes.

The system consists of a white light source, a spatial light modulator, and a visible-to-IR transducer to produce the simulated far-IR scene. While a similar system has been constructed in the past, it used a coherent laser source. Previous laboratory work ignored the radiometric variation across the scene and its effect on the final image. Since the simulation system is computer driven, the scene parameters can easily be altered to allow simulation of various far-IR scenes.

An analysis of the performance parameters and radiometry to simulate a far-IR scene more accurately are proposed. Included in this analysis is a measurement of the spatial resolution (as measured by MTF) and experimental results of different ambient temperatures on the systems dynamic range.

2 Background Information

2.1 Thermal Imaging System background

Thermal imaging systems extend our vision into the infrared by making visible the energy naturally emitted by objects at ambient temperatures characteristic of the earth (*i.e.* 270K - 310K).

Natural visible spectrum images are primarily produced by differences in reflectivity of the objects. However, far-IR images are produced primarily by self-emission due to temperature and by emissivity differences. Far-IR imaging systems often suppress the average value of the scene radiance so that only scene variations around the average temperature are displayed. This allows high contrast to be achieved (Lloyd, 1975).

2.2 Far-IR characteristics

All objects at temperatures above absolute zero emit electromagnetic radiation at a rate and with a wavelength distribution that is a function of the temperature of the object. Far-IR radiation consists primarily of self-emitted radiation from vibrational and rotational quantum energy-level transitions in molecules, and secondarily from reflection of radiation emitted from other heated sources. Fundamental to the computation of far-IR radiation is the

Planck blackbody radiation equation. A blackbody is an idealized object that absorbs all incident radiation and reradiates it in a manner characteristic of its temperature. Planck's equation is based on the premise that thermal radiation is generated by linear atomic oscillators in simple harmonic motion which emit energy as a function of the radiation frequency (Lloyd, 1975). Planck's blackbody equation is:

$$M_{\lambda} = \frac{2\pi hc^2}{\lambda^5 (e^{\frac{ch}{\lambda kT}} - 1)} \quad (2-1)$$

where M_{λ} = the spectral radiant emittance (Watts/meter³),
 h = Planck's constant = 6.626×10^{-34} joule seconds,
 k = Boltzmann's Constant = 1.38×10^{-23} joule/Kelvin,
 c = the velocity of light = 3.0×10^8 meters/second,
 λ = wavelength of the radiation (meters), and
 T = blackbody temperature (Kelvin).

Planck's equation can be integrated over wavelength to yield an expression for the radiant emittance. This expression is known as the Stefan-Boltzmann Law:

$$M = \frac{2\pi^5 K^4}{15c^2 h} T^4 = \sigma T^4 \quad (2-2)$$

where

M = the radiant emittance (W/cm), and

σ = the Stefan-Boltzmann constant = 5.678×10^{-12} W cm⁻²K⁻⁴

Figure 2-1 shows the spectral distribution of objects at various temperatures.

The earth's average ambient temperature for soil, water, and vegetation is about 290 K. From Wien's Displacement Law:

$$\lambda_m = \frac{2898}{\text{temperature}} \mu\text{m}^\circ\text{K}/^\circ\text{K} \quad (2-3)$$

where λ_m is the wavelength of maximum spectral radiant exitance (μm), the maximum spectral radiant emittance from

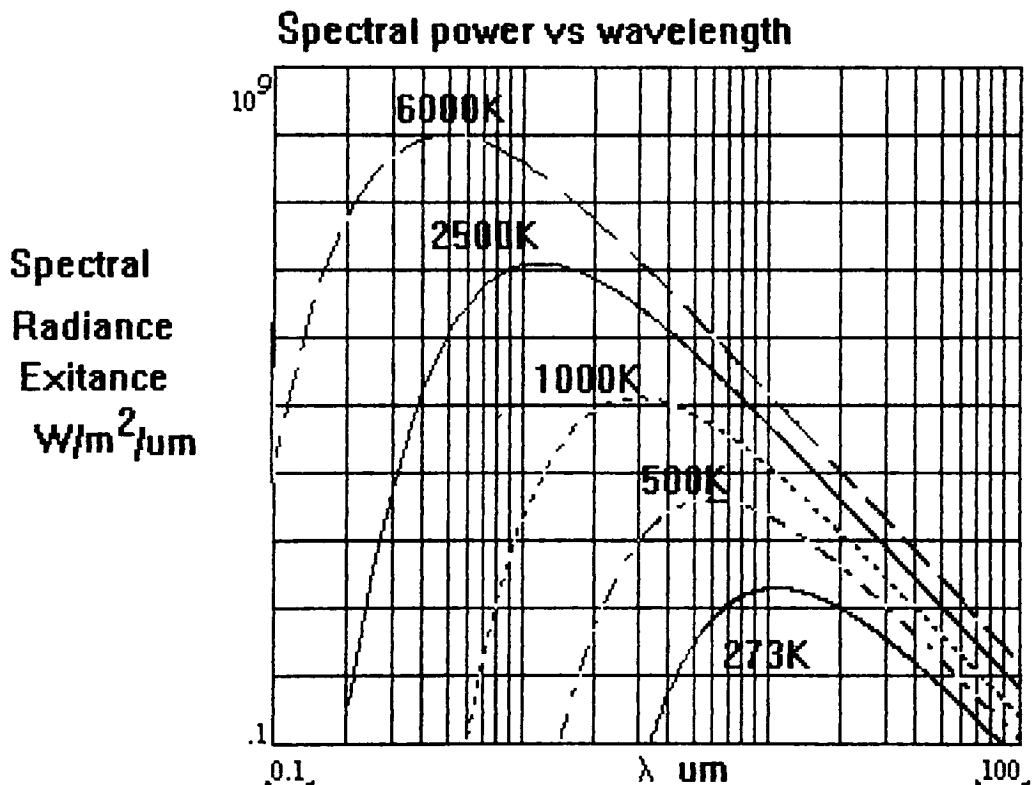


Figure 2-1 Spectral distribution of blackbodies at different temperatures.

earth features occur at wavelengths around 10 μm . The coincidence of the dominant energy emittance of earth ambient temperature objects at around 10 μm and an available atmospheric window makes the far-IR region an ideal region for several commercial and military applications. Man-made objects can have temperatures more than 100K above earth ambient temperature, and thus will emit maximum radiant energy at wavelengths less than that of cooler objects.

These equations describe far-IR radiation from a blackbody. A blackbody provides a standard for comparison of radiation sources that are perfect radiators. Emissivity (ϵ) is the ratio of the radiant emittance M' of an object to the radiant emittance of a blackbody M at the same rature:

$$\epsilon = \frac{M'}{M} \quad 0 \leq \epsilon \leq 1 \quad (2-4)$$

Emissivity has a numeric value that lies between the limits of zero for a non-radiating source and unity for a perfect blackbody. Emissivity is a function of the type of material and its surface finish and can vary with wavelength and the temperature of the material. Greybodies are objects that can be modelled by adding an emissivity term to the above equations.

2.3 Far-IR imaging systems

For an object to be detected in the far-IR region and subsequently recognized and identified, it must produce an apparent temperature difference of sufficient magnitude to distinguish the object from other surrounding objects. The intervening atmosphere must neither excessively blur nor attenuate the received signal. The contributions of scene temperature, reflectivity, and emissivity can be represented in any scene by a single effective temperature value. This is the temperature that would produce the measured irradiance at that point if it were an ideal blackbody radiator. The irradiance measured through an attenuating atmosphere would be equal to that from a body at a lower temperature. The temperature variations of a scene tend to correspond to the details in the visible scene, so a far-IR imaging system provides a visible analog of the far-IR scene (Lloyd, 1975).

The sensor must collect the radiant signal and convert it to an electrical signal in a detector operating in the appropriate spectral band. This electrical signal is then converted to a signal that can be viewed, usually on a video display. The process of converting an infrared scene to a visible scene must be performed so that contours, orientations, contrasts, and details are preserved or

enhanced without introducing excessive noise. Figure 2-2 shows a simple schematic of one possible implementation of a scanning far-IR system. The optical system collects, spectrally and spatially filters, and focuses the radiation pattern from the scene onto a focal plane containing a single detector element.

Electromagnetic radiation from the scene produces changes in some parameter within the detector which ideally is proportional to the energy transported by the field. There are many types of detectors which are sensitive to energy in the 8 to 14 μm range. The detector may be sensitive to the absorbed radiant power or to the number of photons with sufficient energy to alter the carriers within a semiconductor material; some may require cryogenic cooling to operate satisfactorily. There are several ways to scan a far-IR image onto a single detector or a detector array. Further details of detectors and scanners is beyond the scope of this work.

Typically, modern image processing software allows the user to assign colors to each temperature of scanned far-IR images: no true visible color exists for far-IR images. In monochrome systems, hotter objects appear bright or white in the converted image while cold objects appear dark. Objects with intermediate temperatures will appear as various grey

tones. In color systems, temperatures often are assigned colors for ease of interpretation. For computer use, the scene will be quantized into typically 128 or 256 grey levels depending on the system and application. These grey levels are commonly referred to as digital counts (DC) (Warnick, 1990). For this work the scenes will be quantized to 256 grey levels.

2.4 Far-IR Simulation

All far-IR imaging systems must be tested to ensure

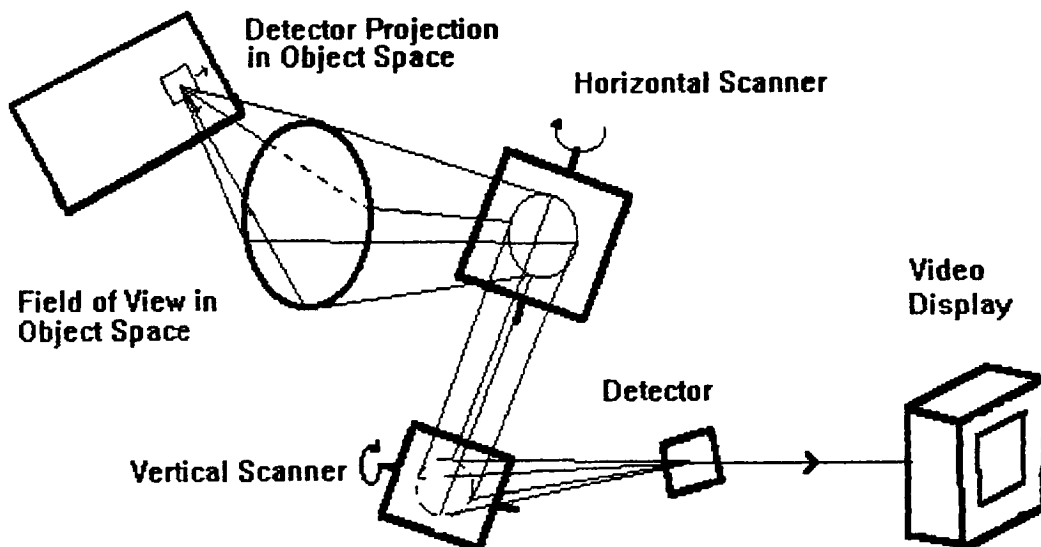


Figure 2-2, A simplified single-detector dual-axis scanner, adapted from Lloyd (1975).

that the desired performance is obtained. Field tests of these imaging systems is often very costly and difficult to reproduce over the range of operational conditions. The output of the imaging detector may be simulated so that all aspects except the optical collection and detection can be verified in the laboratory under controlled conditions. The accurate simulation of far-IR scene that is to be imaged is a more difficult task (Warnick, 1990). The simulated scene should not introduce unreal or troublesome parameters or side effects while duplicating the realistic scene as closely as possible.

Several different technologies are capable of generating a far-IR scene, but each has some drawbacks.

Typically, IR projectors are evaluated in terms of spatial resolution, spectral band, frame rate, dynamic range, temperature resolution, simulated temperature range, flicker, field of view, response time and cross-talk. Frame rate is the frequency at which each element of a scene may be updated to a new temperature. Spatial resolution is defined as the number of independently controlled and equally spaced resolution elements across the projected field-of-view (FOV) at the exit pupil. The FOV of the IR projector should be at least as large as the FOV of the system under test. The spatial resolution of the projector

determines the limit of target and background details. According to the Nyquist criterion, the spatial resolution of the simulator should ideally be more than twice that of the system under test, although an IR projector with a resolution equal to that of the system under test has often been considered satisfactory. The spectral band refers to that portion of the electromagnetic spectrum that the projection system may radiate. The temperature resolution is the minimum temperature difference that can be projected to the system. Response time is the time required for the projector to attain the desired temperature and may be measured as a percentage of the frame time. A response time of ten percent of the frame time is usually acceptable (Hester, 1988). The IR projector requirements can be expected to improve as newer systems are developed (Pritchard, 1988).

The principal characteristics of various IR projector techniques are:

A. Cavity-backed resistor arrays: Electric current is passed through the individual resistor elements which heat up and emit IR energy in accordance with Planck's Law. The cavity-backed devices are monolithic in construction and typically have very small active areas and poor emissivity characteristics. Resistor temperatures of 1000 K have been

demonstrated. However, fill factors of less than 10% and emissivities less than 0.20 degrade the temperature performance substantially. Frame rates on the order of 200 Hz are achievable when the substrate is cooled. The devices are difficult to make and development may be limited to arrays no larger than 256 X 256 elements (Mobley, 1991).

B. Isolated thin-film resistor arrays: They operate in a manner similar to the cavity-back resistor array, but require a complicated processing procedure which limits yields. Resistor temperatures of 700K have been demonstrated. Fill factors are on the order of 50% and emissivities of 0.50 have been achieved. The frame rates are limited to 30-60 Hz, and there is some crosstalk between resistors. Cooling is required. Because of technology limitations, arrays larger than 256 x 256 elements are unlikely (Mobley, 1991).

C. Reflective Liquid Crystal Light Valves (LCLV): A polarized IR source illuminates the liquid crystal material. Depending on alignment of the liquid crystal, the readout is altered and reflected through an analyzer which results in a polarized spatially modulated beam. To reduce flicker, an expensive special-purpose CRT is required to address the liquid crystal. The LCLV has excellent spatial resolution, but suffers from limitations in contrast, dynamic range, and

physical size. Frame rates of 30 Hz are achievable, while the maximum temperature which can be simulated is around 350K (Mobley, 1991).

D. Deformable Mirror Devices(DMiD): DMiDs are made up of individual mirror elements which, depending on the structure, can either be deflected like a piston or tilted along some axis by an electrostatic charge. The IR readout light is modulated by each mirror element based on the amount of energy deflected into collection baffles or out of the line of sight. 256 X 256 element DMids are available with 1000 X 1000 element arrays under development. Frame rates of 500 HZ are possible (Mobley, 1991).

E. Laser Scanner: An infrared laser within the bandpass of the system under test is scanned rapidly across the entrance aperture of the sensor and paints out the IR scene as it progresses. The beam deflection must be synchronized with the readout scan of the sensor under test. Laser scan projectors with resolutions of 128 X 128 have been built. Limits in the modulation system do not allow greater scene resolution at this time. A DMiD system offers high dynamic range and high frame rate. However, it requires a large and complex optical system (Mobley, 1991).

F. IR CRT: IR CRTs emit a high-energy electron beam (e-beam) which is directed at thermal elements on a target

plate. The heated elements emit energy in accordance with Planck's Law. Prototypes have been built and demonstrated. Temperatures in excess of 1000K have been achieved and the device also exhibits good resolution. The target plate elements have no sample-and-hold capability and the e-beam deflection must be synchronized with the sensor under test. Frame rates of 30 to 60 Hz could be achieved, though crosstalk could be a problem. IR CRTs that use a phosphor that emits in the IR region have also been developed (Mobley, 1991).

G. Bly cell: The Bly cell is a visible-to-IR transducer consisting of a very thin blackened membrane housed in an evacuated cell. Because the film is thin, its thermal mass is low. It can respond quickly to changes in visible intensity, and its lateral thermal conduction is low enough to preserve reasonable spatial performance. Visible light projected onto one side is locally absorbed by the membrane and re-emitted in the infrared from both sides. Frame rates of about 30 Hz can be achieved. The device has a limited temperature range, although the use of different materials can increase the temperature range at the cost of lower resolution (Pritchard, 1988).

H. Halftone technology: Electron beam photolithography is used to fabricate a chrome halftone image on a quartz

substrate mask which then has to be transferred to an infrared transparent substrate for IR projection (Pritchard, Ludington, 1992).

Work has been directed at making hybrid systems, usually by optical methods, to project a more realistic IR image. Other systems are available, but will not be considered.

The developed devices may be categorized into three major groups. The devices that modulate infrared sources include thermal films (DMids), liquid crystal modulators, electrostatically deformed mirrors, and film having an IR modulation capability. The second category includes devices that generate a direct infrared scene, such as infrared phosphor cathode-ray tubes and electromechanical diorama simulators. The third category encompasses devices that generate an optically visible image which is transduced into the infrared. The Bly cell falls into this category. Most projectors in the first two categories require some form of scanning or shuttering, which produce a periodic disturbance to the detector circuit that is often intolerable (Woltz, 1988). This project uses a Bly cell.

2.5 Ambient Temperature effects

The maximum temperature attainable by a Bly cell is

limited by its melting point. By cooling the cell a greater temperature range may be achieved.

Driggers et al. (1992), demonstrated that the change in performance of a far-IR imaging system at different ambient temperatures is significant. Most system performance measurements provide a differential temperature for comparison to some factory or field specification. It is uncommon to find a performance specification that is a function of absolute temperature. The problem of test correlation is critical for far-IR imagers, i.e. a far-IR imager performs better in the desert than in the arctic. A larger temperature difference is required in cooler climates to meet an equivalent detector signal of a far-IR imager in a warmer climate. This phenomenon can be demonstrated from the principle of simple blackbody radiometry.

A far-IR detector responds to differences in power. A constant temperature difference does not correspond to a constant power difference. However, Driggers et al. found that a constant power specification can give an equivalent temperature difference as a function of background temperature. The integrated power emitted by a blackbody simulator at temperature T is found from the Stefan-Boltzmann law. Most far-IR imagers are sensitive only in the region of 8 to 14 μm . The bandwidth restriction

requires the integration of Planck's equation to determine the difference in power:

$$\Delta E = \int_{\lambda_1}^{\lambda_2} \frac{C_1}{\lambda^5} \frac{1}{e^{c_2/\lambda T_s} - 1} d\lambda - \int_{\lambda_1}^{\lambda_2} \frac{C_1}{\lambda^5} \frac{1}{e^{c_2/\lambda T_B} - 1} d\lambda \quad (W/m^2) \quad (2-5)$$

Where T_B and T_s are the background and source temperatures in Kelvin, while $C_1 = 3.7413 \times 10^8 \text{ W } \mu\text{m}^4/\text{m}^2$ and $C_2 = 1.4388 \times 10^4 \text{ } \mu\text{m K}$ are Planck's radiation constants. The emissivity is assumed to be unity for the blackbody source analysis. This integration does not yield a closed-form solution, but may be solved by numerical integration.

To have the same power at different background temperatures, the power at ambient temperature must equal the power at the other background temperature. Driggers et al. analyzed the power differences and found equivalent temperature arrangements that allowed the production of several curves showing the equivalent ΔT vs. background temperature for various differences in ambient temperature. Figure 2-3 shows the curve obtained for a ambient $\Delta T = .2^\circ\text{C}$.

Warnick (1990) measured the NE ΔT of the Inframetrics far-IR imaging camera which is used in this experiment: NE $\Delta T = 0.06^\circ\text{C}$. By using Drigger's technique and this NE ΔT value, $\Delta T = .06$ at 298K, and $\Delta T = 0.1$ at 273 K. If the Bly cell is cooled, then a larger temperature range is required to produce the same number of grey levels.

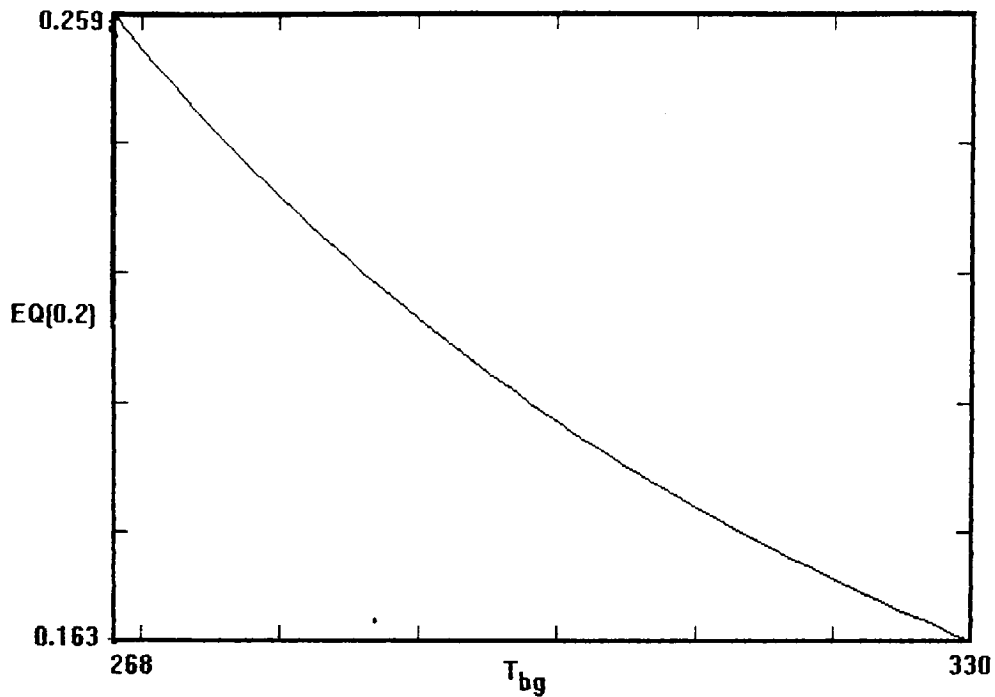


Figure 2-3, T_{bg} is background temperature, and $EQ(0.2)$ shows the temperature differentials required to have the same power as a 0.2 °C temperature differential at 298 °C.

The temperature range of the Bly cell is limited by the melting point of the materials in the membrane. At lower temperatures, less power is emitted by a blackbody. From the Stefan-Boltzmann equation, the total emitted energy is .04478 W/cm² at an ambient temperature of 298K. At a background temperature of 273K, the total emitted energy is .02717 W/cm². A decrease in ambient temperature will increase the temperature range of the Bly cell but will also decrease the number of resolvable grey levels. Conversely, by increasing the temperature range the number of resolvable

grey levels is increased. The theory indicates that decreasing the ambient temperature of the Bly cell from 298 K to 273 K will result in an increased temperature range and the same number of resolvable grey levels.

2.6 Radiometry

This paper is concerned with the transfer of radiative energy between surfaces in three-dimensional Euclidean space. Therefore, the use of solid angles is essential in radiometric calculations.

A common definition of solid angle (Ω) is the three-dimensional angular spread at the vertex of a cone measured by the area intercepted by the cone on a unit sphere (Figure 2-4). This definition gives rise to the unit of the steradian for measuring solid angle. The subtended solid angle in steradians is the ratio of the area of the spherical surface intercepted by the cone to the square of the radius of the sphere. It can be shown that $\Omega \approx A/r^2$, where A is the area A at distance r. The total area of a spherical surface is $4\pi r^2$, so a spherical surface subtends 4π steradians (sr).

The incremental solid angle is calculated from:

$$dA_s = (r d\theta) (r \sin\theta d\phi) = r^2 \sin\theta d\theta d\phi . \quad (2-6)$$

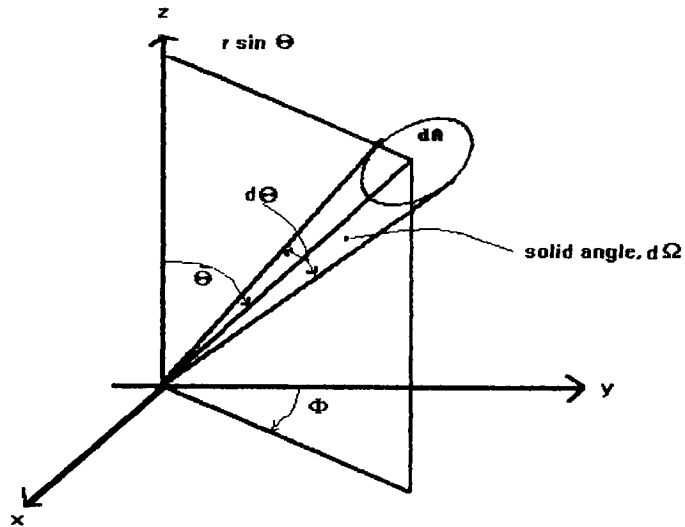


Figure 2-4, Solid angle

The incremental solid angle ($d\Omega$) is

$$d\Omega = \frac{dA_s}{r^2} = \sin\theta \, d\theta \, d\phi \quad (\text{sr}) . \quad (2-7)$$

The total solid angle, Ω is obtained by integration over the angles:

$$\Omega = \int \int \sin\theta \, d\theta \, d\phi . \quad (2-8)$$

For a spherical surface intersected by a right circular cone symmetric about the z axis:

$$\Omega = \int_0^\theta \int_0^{2\pi} \sin\theta \, d\theta \, d\phi = 2\pi (1 - \cos\theta) . \quad (2-9)$$

This equation provides a simple formula for calculating

the solid angle subtended by a sector of a spherical surface with circular symmetry when the associated cone subtends a plane angle of 2θ , ($0 \leq \theta \leq \pi/2$). The angle subtended by any surface (spherical or not) of area A at distance r is:

$$\Omega \approx \frac{A}{r^2} \text{ (sr)}. \quad (2-10)$$

In general, it is necessary to consider the geometry of the source-detector system when calculating the signal incident on the detector. If the source is sufficiently well collimated so that all emitted radiation falls on the detector, only the power emitted by the source need be known. However, in most cases the detector intercepts only a small fraction of the radiated signal.

By treating the detector surface as a collection of plane surfaces, the incremental power incident on an element of the detector dA_d due to the element dA_s of the source is given by:

$$d\Phi = \frac{L_s dA_s \cos\theta_s dA_d \cos\theta_d}{R^2}. \quad (2-11)$$

Where L_s is the source radiance in W/sr/m^2 . For the case of a planar source and a planar detector, both normal to the optical axis, the total flux is:

$$\Phi = \frac{L_s A_s A_d}{R^2} \left(\frac{\text{W}}{\text{m}^2} \right) \quad (2-12)$$

$A_d \ll R^2$ in most cases, and the equation simplifies to $\Phi = L_s A_s \Omega_d$. The product $A_s \Omega_d$ is known as the optical throughput.

Other useful quantities can be defined in terms of the solid angle. As illustrated in Figure 2-5, the *radiant intensity* (or simply *intensity*) of a source (I) is the emitted power per unit solid angle:

$$I = \frac{d\Phi}{d\Omega} \quad \left(\frac{W}{sr} \right). \quad (2-13)$$

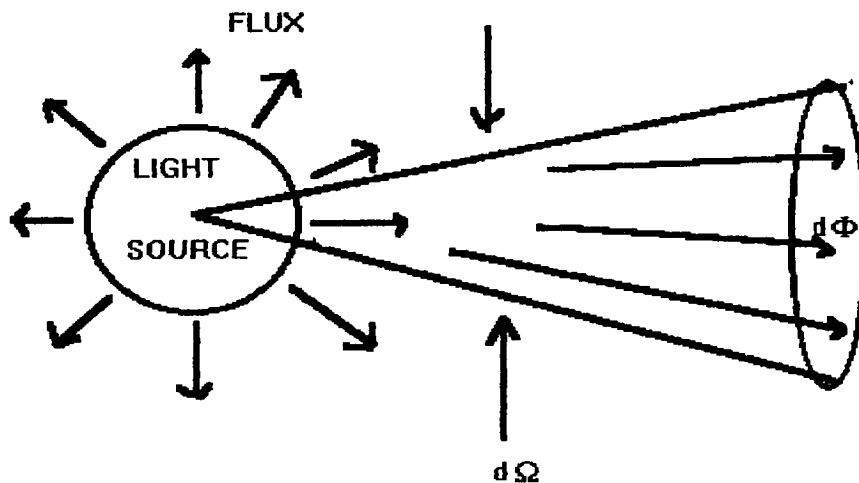


Figure 2-5 Intensity is the emitted power per unit solid angle

The *radiant emittance* or *exitance* (M) of a source is the power emitted per unit surface area: as illustrated in figure 2-6. The *radiance* of a source (L),

$$M = \frac{d\Phi}{dA} \quad \left(\frac{W}{m^2} \right) \quad (2-14)$$

is the emitted flux per unit solid angle, per unit projected area of the source normal to the direction of observation (figure 2-7):

$$L = \frac{d^2\Phi}{d\Omega \cos\theta dA} \quad (W/sr/m^2) \quad (2-15)$$

where θ is the angle between the normal to the plane of the source and the direction of observation. For most cases, L

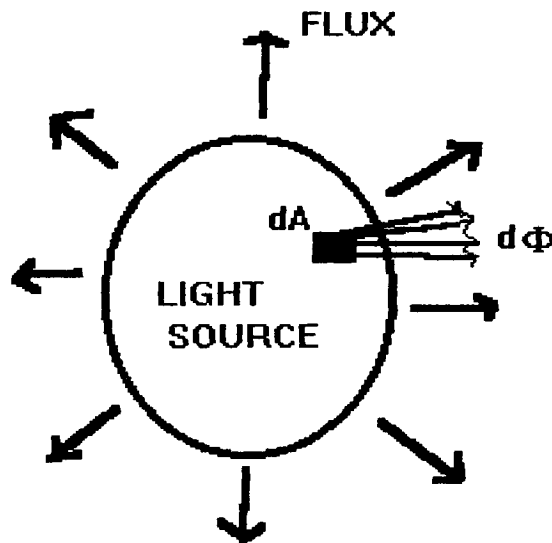


Figure 2-6 Exitance of a source is the power emitted per unit surface area of the source

is a function of the direction of observation. A source for which L is independent of direction is called a Lambertian

source. The Lambertian source is an idealization that does not exist, but some diffusing surfaces may approximate Lambertian behavior over a restricted range of angles. The Lambertian approximation usually is acceptable when used for diffusely illuminated objects. For this project, the illumination over one cell of the liquid crystal display is assumed to be uniform and Lambertian over its viewing angle. Otherwise the exitance from each cell would have to be measured with respect to viewing angle and intensity. The

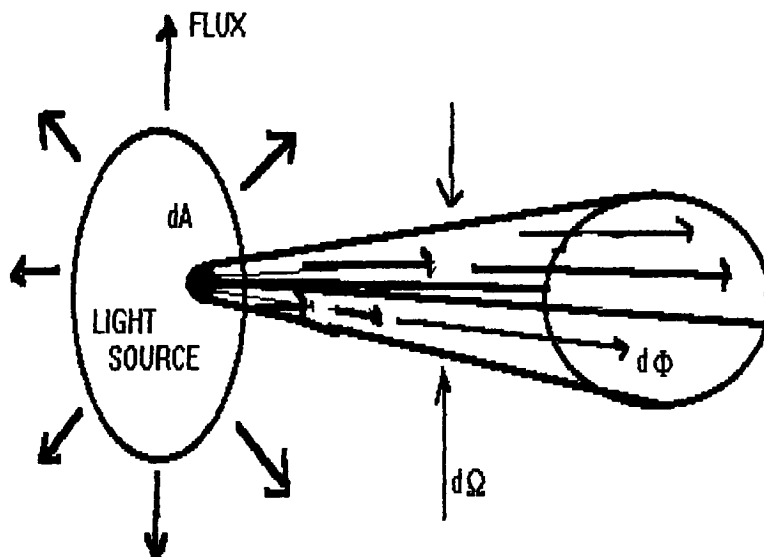


Figure 2-7 Radiance is the emitted flux per unit solid angle, per unit projected area of the source

irradiance of a receiving surface (E) is the power per unit

receiving area:

$$E = \frac{d\Phi}{dA} \left(\frac{W}{m^2} \right) \quad (2-16)$$

as illustrated in figure 2-8.

The total transmitted flux emitted by a Lambertian source into a cone is related to the incident flux Φ_i through $\Phi_t = \Phi_i T$, where T is the transmissivity of the surface. The irradiance on an area that subtends a solid angle at the source requires that the flux emitted within the solid angle enclosed by a cone of half-angle α has to be found. Consider a source element dA , and let $d^2\Phi$ be the

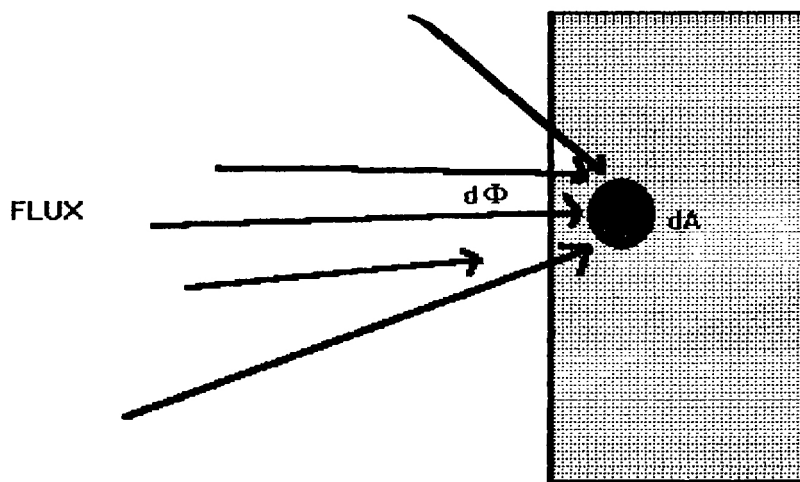


Figure 2-8 Irradiance on a surface is the flux per unit area

flux radiated into the incremental solid angle $d\Omega$. From the definition of radiance we then have

$$d^2\Phi = L \, dA \cos\theta \, d\Omega \quad (2-17)$$

where L is the source radiance either from a light source or from a LCD cell. The solid angle $d\Omega$ is

$$d\Omega = \frac{L \, dA}{2} \int_0^{2\pi} \int_0^\alpha \sin 2\theta \, d\theta \, d\phi = \pi L \, dA \sin^2 \alpha. \quad (2-18)$$

The flux radiated into a hemisphere is found by setting $\alpha = \pi/2$ so that:

$$d\Phi = \pi L \, dA. \quad (2-19)$$

The radiant exitance of a source is $d\Phi/dA$, so combining equations 2-14 and 2-19 yields the radiant exitance of a Lambertian source:

$$M = \pi L \left(\frac{W}{m^2} \right). \quad (2-20)$$

If $E \, W/m^2$ are incident on a diffuse transmitting surface, the radiance of the surface can be found from

$$L = \frac{M}{\pi} = \frac{ET}{\pi} \quad (W/m^2/sr). \quad (2-21)$$

All of these relations were derived for a source element dA , but are approximately true for a small source of finite size, such as an LCD cell.

The flux through an LCD element is collected and imaged by a lens. The flux collected by the lens is determined by its projected size. Consider a small Lambertian source of area ΔA and radiance L centered on the optical axis of a lens. The entrance pupil of the lens subtends an angle of 2β at the source as illustrated in figure 2-9. The flux radiated into the solid angle defined by the rim of the entrance pupil is:

$$\Delta\Phi = \pi L \Delta A \sin^2\beta . \quad (2-22)$$

The irradiance of the image is found by considering a small rectangular Lambertian source of area A_{source} . The flux $\Delta\Phi$

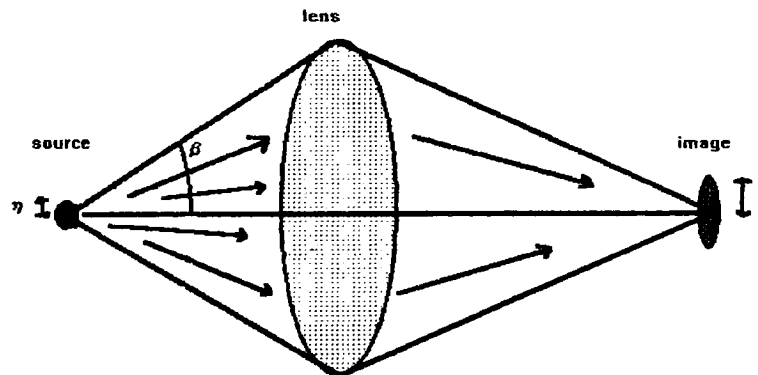


Figure 2-9 Flux collected by a lens

collected by the lens is $\pi L A_{\text{source}} \sin^2\beta$. For a lens in air

with transmittance τ , a flux equal to $\tau \Delta \Phi$ will be transmitted through the lens and be spread over the image area A_{Img} . Thus, the image irradiance is:

$$E = \frac{\tau \Delta \Phi}{A_{\text{Img}}} = \pi \tau L \sin^2 \beta \frac{A_{\text{Source}}}{A_{\text{Img}}} . \quad (2-23)$$

The image irradiance is a function of the source radiance and projected size and transmission of the lens. Lens aberrations spread the image irradiance over a larger area. If the lens reflects or absorbs some of the incident radiation, the irradiance is further reduced.

Several problems may affect image quality, including aberrations of the optics, a poorly collimated light source, nonuniformities in the Bly cell or liquid crystal display, and nonlinearities of the LCD response. An illustration outlining the components affected by these problems in this project is given in figure 2-10.

The irradiance equation derived above may be modified to include the spatial dependence of the system components:

$$E(x, y)_{\text{Bly}} = \pi \tau(x, y)_{\text{Lens}} L(x, y)_{\text{SLM}} \sin^2 \beta \frac{\Delta A_{\text{SLM}}}{\Delta A_{\text{Bly}}} . \quad (2-24)$$

This equation can be further expanded to yield:

The exitance from the Bly cell can be found from the above equation by:

$$E(x,y)_{Bly} = E(x,y)_{SLM} \tau(x,y)_{SLM} \tau_{Lens} \sin^2 \beta \frac{A_{source}}{A_{Bly}} . \quad (2-25)$$

$$M(x,y)_{Bly} = E(x,y)_{Bly} a(x,y)_{Bly} . \quad (2-26)$$

Where $a(x,y)$ is the spatially dependent absorption of the Bly Cell.

In this project, it is desirable to modify the input image to compensate for radiometric nonuniformities across the scene.

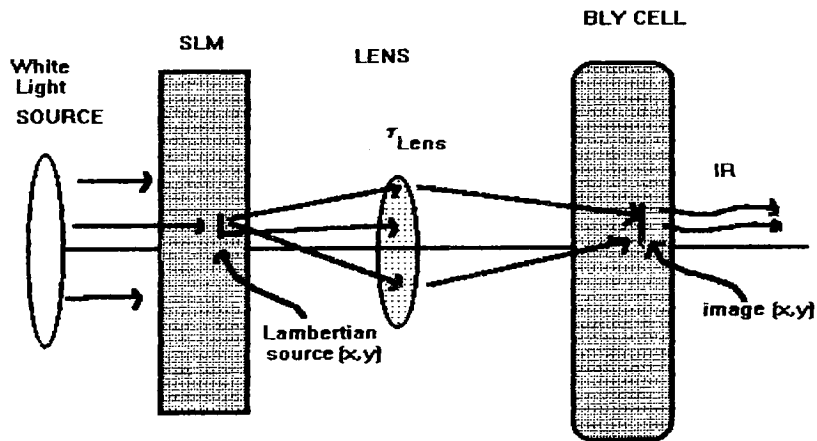


Figure 2-10 System components affecting radiometry

2.7 Optical Transfer Function

Some of the earliest optical systems were telescopes for astronomy. Stars provided nearly ideal point sources which became the standard test object for optical systems. The image of a point source is called the point spread function (psf) of the system. The point spread function is the mathematical expression for the flux-density distribution in the image of a point source. Similarly, the line spread function (lsf) is the mathematical expression for the flux-density distribution in the image of a line source. Point-source images still are used for evaluating the response of image-forming systems.

The optical transfer function (OTF) represents a recent approach to characterizing systems. The characteristics that give the OTF an advantage over other means of evaluating image quality are:

- A. The OTF is linear.
- B. The OTF requires no specific light source assumptions about the shape of the aperture stop.
- C. The OTF is a direct application of the Fourier transform theory in which a two-dimensional variation of intensity over the object plane is analyzed into a two-dimensional spectrum as spatial frequencies. The OTF then describes how each of these Fourier components

is attenuated in amplitude and shifted in phase as it appears in the image.

- D. The OTF can be both calculated directly from the design data of any system and measured for that system after fabrication (Williams, Becklund 1990).

Direct measurement of the OTF for an image-forming optical system has several practical difficulties:

- A. Sinusoidal patterns of constant contrast are difficult to make.
- B. Design limitations tend to restrict the range of spatial frequency of test systems to less than desired. Also, an equivalent test near zero frequency is difficult to attain.
- C. Practical light signal levels at the detector often are low enough to be disturbed by ambient light.
- D. Illumination of the object has to be truly incoherent. Even a small degree of coherence would produce an incorrect result (Williams, Becklund 1990).

Due to these difficulties, the OTF seldom is measured directly but actually is derived from some other optical parameter. The OTF can be calculated by interferometric experiments or by scanning the appropriate image in test

setups for measuring the point spread function, the line spread function, or the edge trace (Williams, Becklund 1990).

To express magnitude and phase simultaneously, the OTF is put in complex form:

$$OTF(\omega) = |OTF(\omega)| e^{i\Phi(\omega)} = T(\omega) e^{i\Phi(\omega)}, \quad (2-27)$$

in which $T(\omega)$ is the modulation transfer function (MTF) which is defined as the magnitude of the OTF and $\Phi(\omega)$ is the phase transfer function (PTF).

Point sources of light are easy to visualize and to

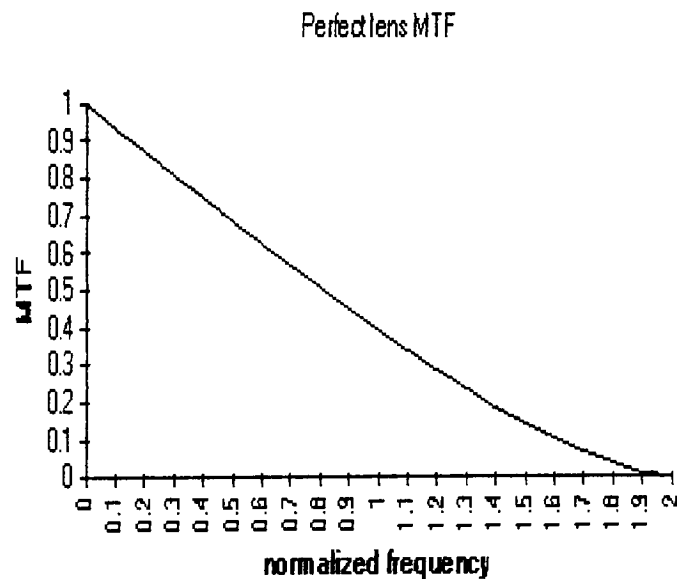


Figure 2-11, The MTF for a diffraction-limited lens in incoherent light. The PTF is zero for all frequencies. From Williams, Becklund, 1990.

analyze, but cannot be realized in practice. For practical purposes, a source of finite dimensions is a point source if its dimensions are negligible compared to other significant dimensions in the optical configuration. The image of a point source is always larger than the point source due to diffraction and other factors, e.g. dust particles or scratches on optical surfaces, foreign particles within lens material, irregularities on the edge of the aperture stop, and aberrations (including defocusing).

Because the line spread function is easier to measure, it is usually preferred over the point spread function in optical analysis. It can be shown that the Fourier Transform of the line spread function is one line of the optical transfer function. Following Gaskill's (1978) development of the lsf, with the operator $\mathcal{E}[\cdot]$ describing an arbitrary two-dimensional linear shift invariant system, the impulse response $h(x,y)$ of the system is defined by

$$\mathcal{E}[\delta(x,y)] = h(x,y). \quad (2.28)$$

Assume the optical system has a point spread function (psf) $h(x,y)$ and OTF $H(\xi,\eta)$, both of which are unknown. Apply as an input a line mass located along the y-axis, i.e.

$$f(x,y) = \delta(x). \quad (2.29)$$

The output is the line spread function $l(x)$ which can be

expressed in terms of the unknown psf and OTF as

$$\begin{aligned} l(x) &= \delta(x) ** h(x, y) \\ &= \int_{-\infty}^{\infty} h(x, B) dB, \end{aligned} \quad (2.30)$$

where $**$ is the convolution operator. By using a Fourier Transform theorem, the one-dimensional Fourier Transform of the lsf is

$$L(\xi) = \mathcal{F}[l(x)] = \mathcal{F}\left[\int_{-\infty}^{\infty} h(x, B) dB\right] = H(\xi, 0). \quad (2.31)$$

Several methods can be used to obtain a line spread function. One method of obtaining the line spread function is to differentiate the edge spread function (esf) which results from inputting an edge trace into the system.

Following Gaskill's (1978) development of the esf, for a rotated x, y coordinate system in which the edge is along the y -axis, the esf $e(x)$ can be described as

$$\begin{aligned} e(x) &= \mathbb{E}[\text{step}(x)] \\ &= h(x, y) ** \text{step}(x) \\ &= \int \int_{-\infty}^{\infty} h(\alpha, B) \text{step}(x - \alpha) d\alpha dB \end{aligned}$$

$$\begin{aligned}
&= \int_{-\infty}^{\infty} l(\alpha) \text{step}(x-\alpha) d\alpha \\
&= l(x) * \text{step}(x) .
\end{aligned} \tag{2.32}$$

By using Fourier Transform theorems equation 2.32 can be rewritten as

$$e(x) = \int_{-\infty}^x l(\alpha) d\alpha . \tag{2.33}$$

From equation 2.31 the relation between one line of the OTF and the lsf can be expressed as the Fourier Transform of the lsf:

$$OTF(f) = \int_{-\infty}^{\infty} l(x) e^{-j2\pi fx} dx . \tag{2.34}$$

The relation between the lsf and esf from equation 2.33 can be rewritten as

$$l(x) = \frac{de(x)}{dx} . \tag{2.35}$$

Combining equations 2.34 and 2.35 and using the derivative theorem of the Fourier Transform the relationship between one line of the OTF and the esf can be written as

$$OTF(f) = j2\pi fE(f) , \tag{2.36}$$

where $E(f)$ is the Fourier transform of the esf $e(x)$.

The esf is obtained by scanning the image of a point source with a knife edge (figure 2-12). Closer examination reveals that the transition region has finite width due to diffraction, aberrations, and defocusing. The esf and the lsf are mathematically equivalent manifestation of the optical system and thus one can be transformed into the other. The esf can be viewed as either the semi-infinite integral of the lsf or the convolution of the line spread function and a step function (Williams & Becklund, 1990).

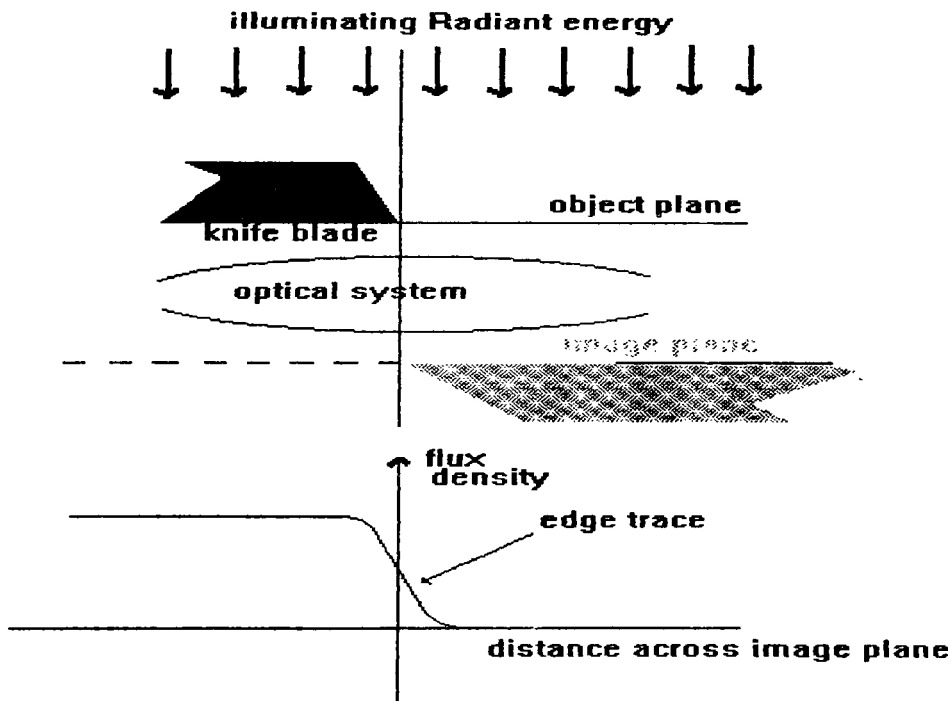


Figure 2-12 Schematic showing the formation of an edge trace adapted from Williams, Becklund, 1990.

The MTF describes the ability of the system to transmit modulation to the output, while the PTF describes the translation of sinusoids at each spatial frequency. It is common practice to specify only the MTF since most MTF curves exhibit significant attenuation of the high-frequency components. This has the effect of minimizing any distortion caused by a shift in phase. The combined effect of a small value of the MTF and the reduced actual shift due to short wavelengths at these frequencies make the PTF characteristic unimportant for most applications.

Warnick (1990) describes a far-IR simulation system that employed a visible laser source, a spatial light modulator, and a Bly cell to create a self-emitting thermal IR scene. The work presented here is modeled on that system but has been modified to include an improved spatial light modulator and a white light source. In order to produce a more accurate IR image, this project will try to compensate for radiometric variations across the output scene by changing the input scene. The design of this system is reviewed in the next section. It is expected that by using a better spatial light modulator that the spatial resolution can be improved. The effect of decreasing the ambient temperature on the thermal contrast of the system will also be investigated.

3.0 Design of Far IR Simulation System

The far-IR simulation system uses a visible white light source, optics, and digital image processing to create a visible image of a scene. This visible scene is converted to a far-IR image through the use of a visible-to-IR

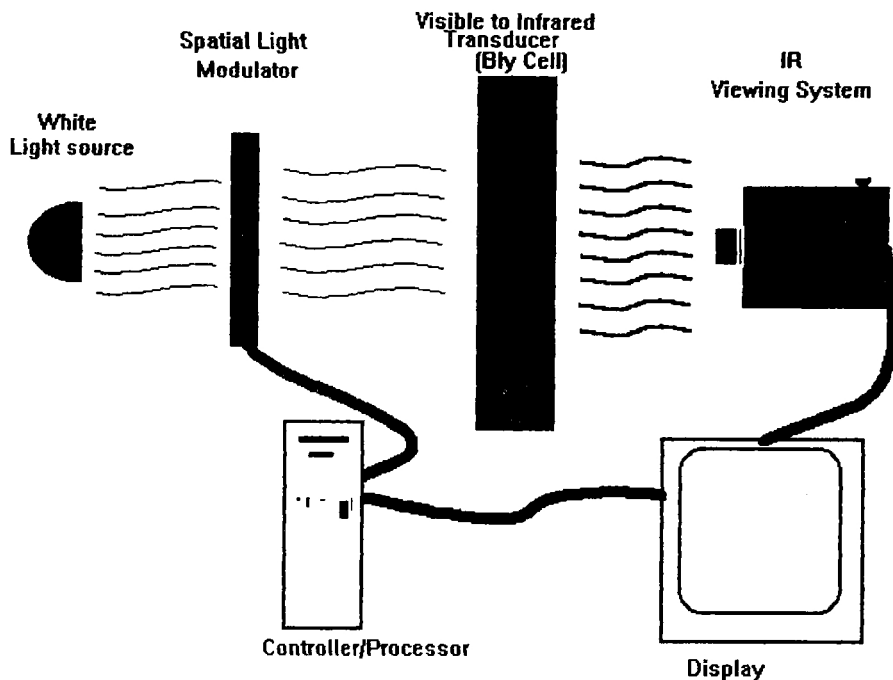


Figure 3-1 Block diagram of simulation system setup
transducer

(VIRT). A block diagram of the basic components is shown in Figure 3-1. By modulating visible light and then converting it to infrared at the last stage readily available optical

elements could be used. Furthermore, system alignment is easier when using visible light.

In this section, each component will be described individually.

3.1 Energy Source

The energy for the far-IR simulator is supplied by a 1000W tungsten-halogen incandescent bulb in a parabolic reflector. The light source is not perfectly collimated and generates a significant amount of heat. The light source variations across the scene could be reduced by adding a diffuser at the cost of reduced signal power. A gradient filter could be used to compensate for the decrease in light intensity towards the corners. Variations in the light intensity across the image plane can also be compensated by preprocessed radiometric corrections through the adjustment of the pixel values of the LCD.

3.2 Spatial Light Modulator

Polarized light is spatially modulated to create a visible image of a scene. The spatial light modulator (SLM), is similar to a photographic slide in a slide projection system which creates a visible image by the selective spatial transmission of light to a projection

screen. The SLM used is a liquid crystal display (LCD) from an Epson video projector. Similar devices have been used successfully as spatial light modulators for optical pattern recognition (Gregory and Kirsch, 1992), real-time optical signal processing (Hughes, 1987, Yu, et al., 1986, Young, 1986, and Liu, 1985) and for self-emitted scene generation (Warnick, 1990). Specifications for the SLM used for this work are contained in Appendix A and a general overview of the Epson system is found in Kirsch et al. (1992), while the addressing system is reviewed by Cotariu et al. (1992), and Clark et al. (1992).

Each pixel is a single liquid-crystal cell. Liquid crystallinity is a fluid state of matter. A twisted liquid crystal cell is a thin layer of nematic liquid crystal placed between two parallel glass plates and rubbed so that the molecular orientation rotates helically about an axis normal to the plates. The polarization plane of linearly polarized light travelling in the direction of the axis of twist rotates with the molecules, so that the cell acts as a polarization rotator (figure 3-2). The twisted liquid crystal cell placed between crossed polarizers can be operated as an analog modulator. At intermediate tilt angles, there is a combination of polarization rotation and wave retardation. The analysis of the transmission of

polarized light through tilted and twisted molecules is beyond the scope of this work, but the overall effect is a partial intensity transmittance. There is an approximately linear transition between the total transmission of the fully twisted (untilted) state and zero transmission in the fully tilted (untwisted) state (Saleh and Teich, 1991). For this work, the linearity assumption was not found to be good enough. Instead the range is modelled by a quadratic equation.

Each LCD has 220 lines of 320 pixels and a clear aperture of 1.25 inches. Each pixel measures 55 X 60 μm with a center-to-center spacing of 80 X 90 μm ; the active area is 46%. The transmission efficiency of the device is about 43% at $\lambda = 0.6328 \mu\text{m}$ (Kirsch et al. 1992). Testing confirmed the findings of Cotariu et al. (1992) that 20 lines at the top and bottom of a 512 x 480 digital input image are not displayed. The two fields of 220 lines are written to the same 220 lines on the LCD. Pixels at the beginning and end of the horizontal lines are ignored resulting in approximately 493 of the 512 horizontal image pixels being resampled onto the 320 horizontal LCD cells. This resampling can cause edge blurring as well as aliasing according to Clark et al. (1992).

The LCD was removed from the projector housing and a

long ribbon cable was attached. A video signal and a synchronization pulse from a computer were fed into the drive electronics of the Epson TV. This allows either a dynamic or

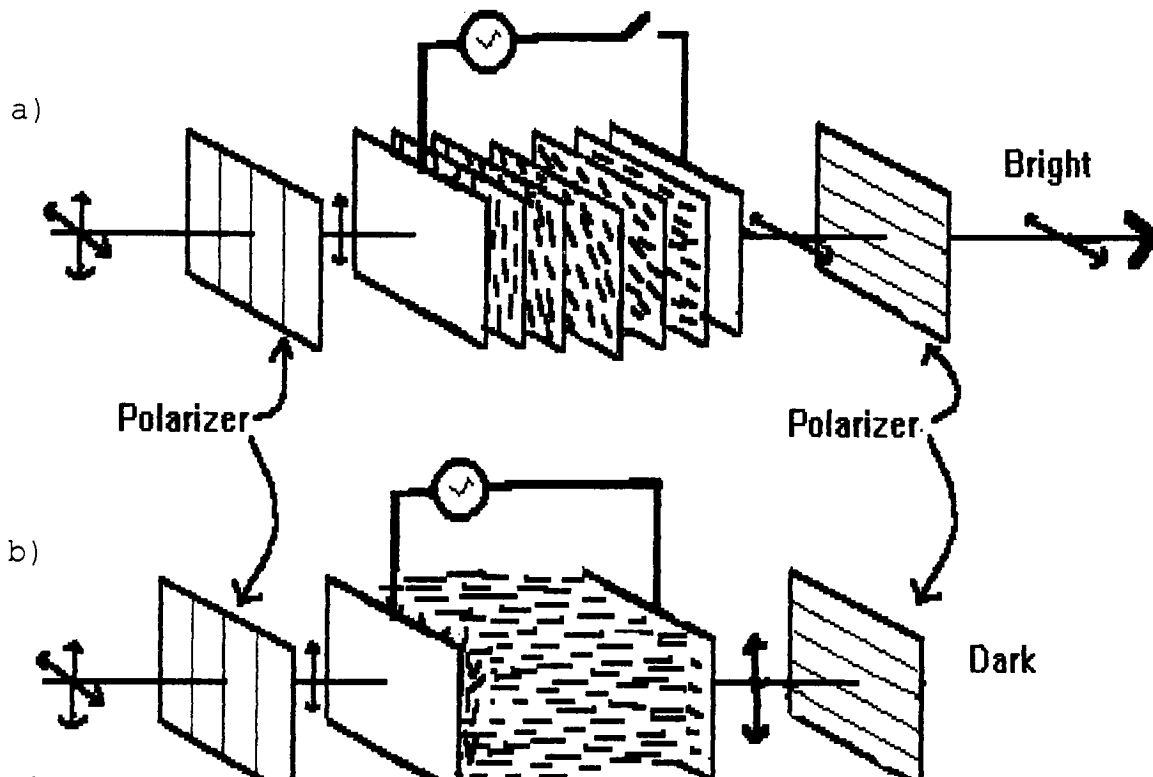


Figure 3-2 (a) Without an electric field the liquid-crystal cell rotates the light. (b) With an electric field the cell's rotatory power is suspended (Saleh, Teich, 1991).

a static input to be displayed. The input images usually are not standard visible scenes, since there is little correlation between visible images and far-IR images. The far-IR scenes can be generated from synthetic thermal models

that account for the temperature, emissivity, and reflectivity of objects, or by using true IR images (Warnick *et al.*, 1990). A description of the process to generate the far-IR scenes is beyond the scope of this work.

According to Cotariu *et al.* (1992, 1993), the operational parameters of the LCD cell are the direction of polarization of the input light, the voltage on the cell, and the angle of a analyzer. These parameters determine the mode of operation: amplitude-mostly mode, phase-mostly mode or a combination. Other researchers have found that the system exhibits greatest contrast when the bias is set to 4.5. Adjusting the input polarizer to about 83° and analyzer to 86° (plus or minus a few degrees) resulted in the highest contrast for intensity measurements (Cotariu *et al.* 1993). These settings result in a mixed-mode operation which is satisfactory for non-coherent illumination.

Clark *et al.* (1992) found that the Epson LCD performance degrades as the irradiance of a laser beam is increased since the Epson device does not rotate all light by the same angle. Initial contrast measurements also indicated that the LCD is not achromatic; with the original dichroic filters, the contrast varied by about 15%. A contrast ratio of 80:1 was found for the SLM with a white light of 150 Watts.

Nematic LCDs in commercial devices typically have a life of about 5 years (Canon EOS 10S camera owners manual). Over this life, the contrast of the device decreases due to chemical changes within the cells. It was also noted that the contrast of the LCD was reduced noticeably after exposing one of the LCDs to high intensity white light without an IR absorbing filter.

An area of concern noted by Clark *et al.* (1993), is the drive electronics which do not allow individual pixel control.

3.3 Optics

Due to the poor collimation of the light source and other physical limitations, several achromatic lenses were used to focus the image. The lenses also could be used to magnify the image. In this project, the positions of the lenses were adjusted for unit magnification.

3.4 Visible-to-IR Transducer

A Bly cell, which is a visible-to-IR transducer (VIRT), is used to convert the visible image to a far-IR signal. A commercially available Bly Cell from Eppley Labs which has been previously used in a similar setup (Warnick, 1990) is described below.

The Bly cell is comprised of a very thin membrane (50 nm) enclosed in an evacuated cell (figure 3-3). The vacuum cell has windows on both sides of the membrane. One window transmits the incident visible energy to the membrane while the other transmits the emitted IR energy from the membrane. The membrane is coated on the input side with a gold-black absorbing film to achieve high absorption (62%) in the visible wavelengths and high emissivity in the far-IR wavelengths. The visible image is projected onto one side of the membrane where it is absorbed and converted to localized heat. Because the heat capacity of the membrane is very low, the surface quickly achieves a stable temperature. In a vacuum, heat is transferred radiatively from both surfaces. Specifications for the VIRT subsystems are given in Appendix B.

The resolution, conversion efficiency, and temporal response of the Bly cell depend on the atmospheric pressure within the cell. Conversion efficiency improves as the pressure decreases down to about 10^{-7} torr (Lee and Snyder, 1988). The operating vacuum chosen results in a compromise between the resolution and speed (Pritchard, 1988). The vacuum in the Bly cell used in this system rose from 5×10^{-6} Torr to 10^{-4} Torr in about one hour. It was not practical

Missing Page

horizontal

directions with mirrors. The digitized output of the Inframetrics system is captured by an Imaging Technologies frame grabber, averaged, stored, and analyzed by using the software in Appendix D. Specifications for the Inframetrics viewing system are listed in Appendix C.

3.6 Radiometric Normalization

Radiometric variations in the image are corrected in software. This method was chosen instead of an optical solution because of its low cost (computer already available) and ability to be easily adapted to correct several system errors. The system errors may be due to variations among LCD pixels, nonuniformities in the Bly cell membrane, and light intensity variations.

The following method is used to correct radiometric variations:

- A. A flat field image of a gray value in the middle of the dynamic range of the LCD is projected through the system. A mid gray value was chosen as this is the region of the LCD response that is most linear.
- B. The resulting image is saved as a reference file.
- C. The average value of this reference image is found and a digital file is created which contains the difference

between each pixel value and the average. This is the image correction file.

D. Input image is modified by software which adjusts each pixel value of the image by an amount corresponding to the value in the correction file for that position. If the input file size is not the same as that of the output file (input image is always larger in this application), then the software will take this into account (i.e. one data point from the correction file may be used to adjust more than one input image pixel). The software also uses the quadratic equations from the LCD response to ensure that the values are properly scaled.

E. The modified input image is then applied to the LCD.

This method will work if the system dynamic range is large enough to allow this compensation and still have enough range left over to display an image. The software to accomplish the radiometric corrections is listed in Appendix D.

3.7 Cooling System

The temperature range of the Bly cell could be improved by cooling the Bly cell. The Bly cell and IR camera were set up inside a commercial freezer with a window

to admit incoming visible energy. The temperature of the freezer was monitored closely and allowed to change only slowly to avoid damage to the Bly Cell. A fan was placed within the freezer to circulate the air to reduce temperature stratification.

The glass on either side of the LCD readily absorbs energy from the white light source and heats up the nematic material. This severely limits the light throughput of the system. Fans were used to cool the LCD and an IR-absorbing filter which was placed in front of the SLM.

4.0 Experimental Methods

The performance of the simulation system was quantified by evaluating images captured by the frame grabber. The digital images were quantized to 256 gray levels which correspond to the different intensity values in the image. The images were used to calculate the system performance via standard techniques. A detailed description of the experimental methods are presented in this section.

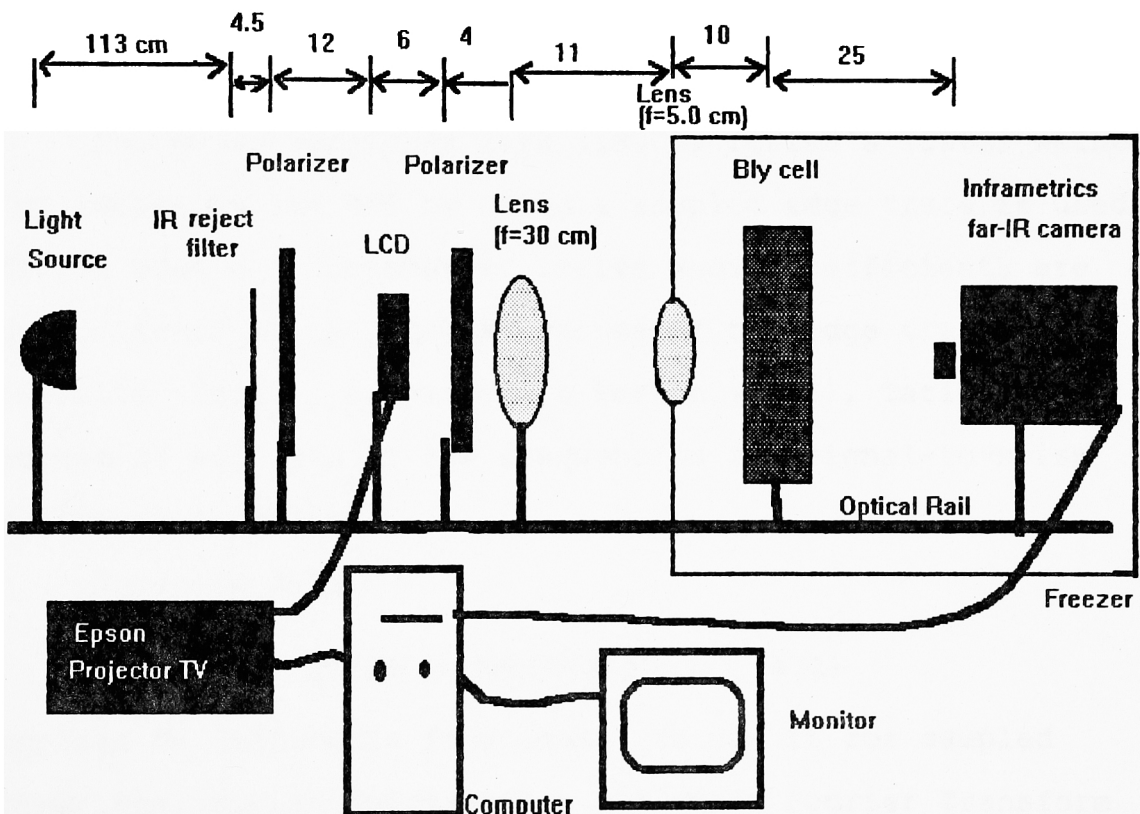


Figure 4-1, System setup showing location of components. Measurements are in cm.

4.1 System setup and Alignment

For ease of accessibility and initial alignment, the system was first assembled on a two-meter triangular optical rail without the freezer. All components were mounted on movable carriers to facilitate component positioning. Following the successful testing of the setup, the system was reconstructed to include the freezer. The final setup is shown in figure 4-1.

4.2 Modulation Transfer Function

Following Warnick's work (1990), Tatian's (1965) method for computing the MTF by using a sampled edge trace is used. Tatian used a trigonometric series whose coefficients are proportional to the sampled values of the edge trace (Warnick, 1990). According to Perron (1988), Tatian's method is accurate at low frequencies for signal-to-noise ratios up to 30 to 1.

Equation 2-36,

$$OTF(f) = j2\pi fE(f), \quad (4.1)$$

applies to continuous functions. To use it for sampled functions, Tatian approximates the exact Fourier Transform by letting $e(n\epsilon)$ represent a sampled edge trace, where n is the sample number and ϵ is the sample interval, then the OTF is given by:

$$OTF(f) = j2\pi f\epsilon \sum_{n=-\infty}^{\infty} e(n\epsilon) e^{-j2\pi fn\epsilon} . \quad (4.2)$$

Since the normalized edge trace function is assumed to be at zero and unity at the sample points denoted by N and M respectively:

$$OTF(f) = j2\pi f\epsilon \sum_{n=N}^M e(n\epsilon) e^{-j2\pi fn\epsilon} + j2\pi f\epsilon \sum_{n=M+1}^{\infty} e^{-j2\pi fn\epsilon} . \quad (4.3)$$

The summation from $-\infty$ to N-1 vanishes since the value of the normalized edge trace is zero. By using the trigonometric identities:

$$\sum_{n=M+1}^{\infty} \sin(nf) = \frac{\cos((N + \frac{1}{2})f)}{2\sin(\frac{f}{2})} , \quad (4.4)$$

$$\sum_{n=M+1}^{\infty} \cos(nf) = \frac{\sin((N + \frac{1}{2})f)}{2\sin(\frac{f}{2})} , \quad (4.5)$$

the OTF can be expressed as:

$$OTF(f) = j2\pi f\epsilon \sum_{n=N}^M e(n\epsilon) e^{-j2\pi f n\epsilon} +$$

$$j2\pi f\epsilon \left(\frac{\sin((M+\frac{1}{2})2\pi f\epsilon)}{2\sin(\frac{2\pi f\epsilon}{2})} + \frac{j\cos((M+\frac{1}{2})2\pi f\epsilon)}{2\sin(\frac{2\pi f\epsilon}{2})} \right). \quad (4.6)$$

The MTF can now be computed by

$$MTF(f) = |OTF(f)|. \quad (4.7)$$

The programs and routines used to implement these computations are listed in Appendix E.

Implicit in Tatian's method is the assumption that the imaging system is both linear and shift invariant. For an image which was sampled over an area larger than the psf of the imaging system, the assumption of shift invariance is not valid (Park et al., 1984). However, Warnick (1990) found that the spatial variance of the Inframetrics/Imaging Technology viewing system was less than 3%. Thus, the apparatus can be assumed to be shift invariant. Radiometric variations cause amplitude variations across the scene which can have an adverse affect on the MTF (Chung and Hopkins, 1989).

4.3 Inframetrics Viewing System

As outlined by Warnick (1990), far-IR images of edges in both the vertical and horizontal directions must be produced due to the different components used to scan the vertical and horizontal directions in the Inframetrics system. A blackbody bar target is used to generate the test edges (figure 4-2) for the viewing system. The blackbody was also used to check the linearity of the system for different input temperatures.

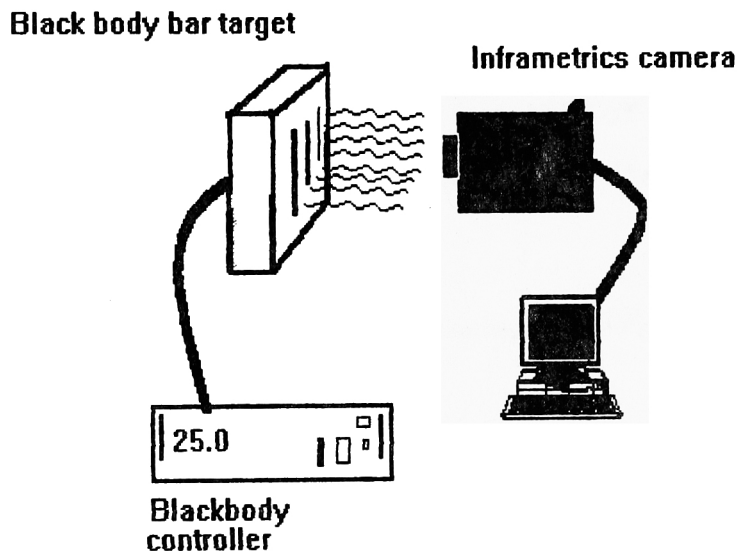


Figure 4-2 Inframetrics viewing system test setup

4.4 MTF of Simulation System

The MTF of the simulation system was measured by applying a high contrast edge image to the SLM. This

measurement was done at room temperature.

Four components affect the MTF of the simulation system: the LCD, polarizers, imaging lens, and Bly cell. Thus, the equation for the system MTF is:

$$MTF_{SYS} = (MTF_{LCD}) \times (MTF_{Polarizer}) \times (MTF_{Optics}) \times (MTF_{VIRT}) . \quad (4.8)$$

The polarizers will be included with the spatial light modulator (SLM). The white light source does not affect the system MTF as it is not in the imaging chain. Nonetheless, certain components of the illumination system (e.g. coherence and amplitude variation of the light) may adversely affect the MTF. The MTF of the image will also depend on the MTF of the viewing system. Thus the observed MTF shall be:

$$MTF_{Observed} = MTF_{Inframetrics} \times MTF_{System} . \quad (4.9)$$

By rearranging this, the MTF of the system is:

$$MTF_{System} = \frac{MTF_{Observed}}{MTF_{Inframetrics}} . \quad (4.10)$$

Due to the different sizes of the pixels in the horizontal and vertical directions of the SLM, the MTF of the simulation system will have to be measured in both orientations.

The MTF of the SLM and the Bly cell were calculated to identify the limiting component of the system. The measurement of the MTF of the Bly cell by Warnick (1990) was used to check the validity of the current measurement.

4.5 Measurement of Noise-Equivalent temperature change

The Noise-Equivalent Delta Temperature (NE Δ T) is a measure of the thermal resolution of the simulation system. To resolve a grey-level transition in the far-IR output image, the change in gray levels must be larger than the NE Δ T of the simulation system. For example, if the NE Δ T of a system is 0.5°C and the maximum thermal contrast is 20°C, then the number of resolvable grey levels is 40.

Warnick(1990) found that the Inframetrics viewing system has the lowest NE Δ T of the available sensors. The NE Δ T of the test equipment should be less than that of the system.

4.6 Measurement Procedures

Before the parameters of the simulation system can be quantified, several performance and calibration measurements of the test equipment and setup were made. The output image is a 512-by-460 array of gray values in the range 0-255, which are proportional to the amplitude at each sample

point. These integers can be converted to temperatures by using a calibrated source to find the appropriate LUT. In areas free from defects, the VIRT is assumed to have a constant emissivity, thus all radiance contrasts should be due to temperature differences. The Bly cell was evacuated to 5.5×10^{-5} torr before each use.

The polarizers were adjusted to give maximum contrast for a bilevel image of maximum dynamic range: the letter "E" which was made of pixel values of 255 against a background of zero.

To characterize the linearity of the system, several flat-field images of various values were applied to the system. These images were analyzed to determine how the input grey levels have to be modified to obtain a linear response. After doing this for several pixel levels an equation describing the variations was found by using regression techniques. The appropriate equation is then implemented by applying it to the input image.

Radiometric variations across the image plane can be measured by applying a constant value to the SLM and capturing the resulting image as outlined in section 3.6. Any significant variations across the SLM, source, Bly cell, or Inframetrics camera were compensated at the same time. To reduce the noise in the output images, several frames

were averaged by using the available frame grabber software.

All images were from other sources as the generation and enhancement of IR images is beyond the scope of this work.

To see if there might be an improvement in the system dynamic range when the Bly cell is cooled, the dynamic range of the system was measured at several temperatures.

The results from the procedures carried out are listed in section 5.

5.0 Results

The major system components were evaluated by measuring their MTFs. The overall system was evaluated by its MTF and maximum thermal contrast. The results of these performance measurements are presented in this section.

5.1 Spatial Light Modulator

The vertical and horizontal MTFs of the SLM were found by applying an "E" to the LCD and viewing the image with a CCD camera. Figure 5-1 shows the image, while figures 5-2 through 5-5 show the horizontal and vertical MTFs and the data used to derive them.

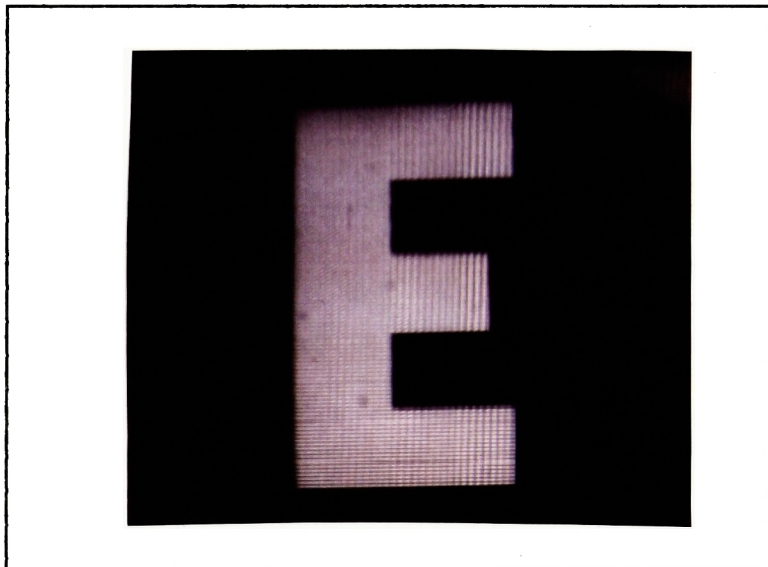
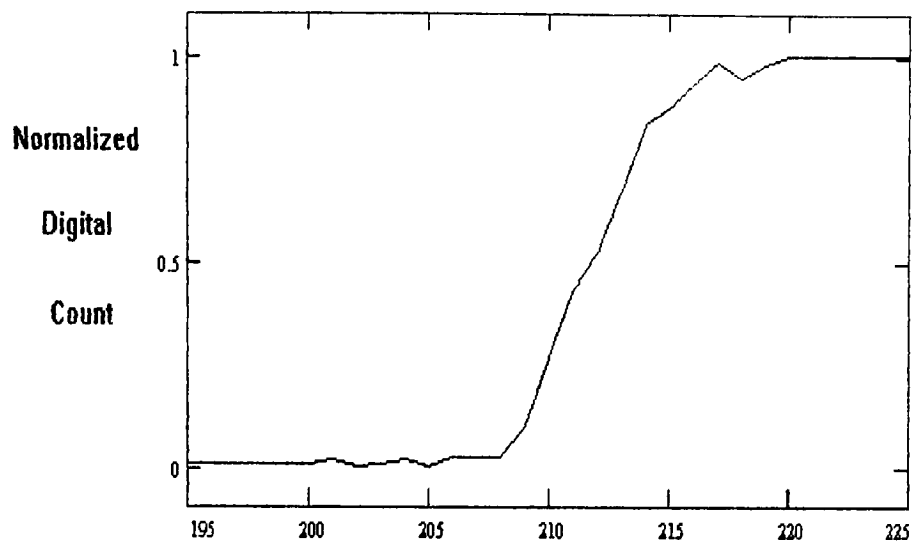


Figure 5-1 - Image on SLM used to evaluate spatial resolution



Vertical LCD Pixels averaged over 50 columns

Figure 5-2 - Normalized vertical LCD pixel values from figure 5-1.

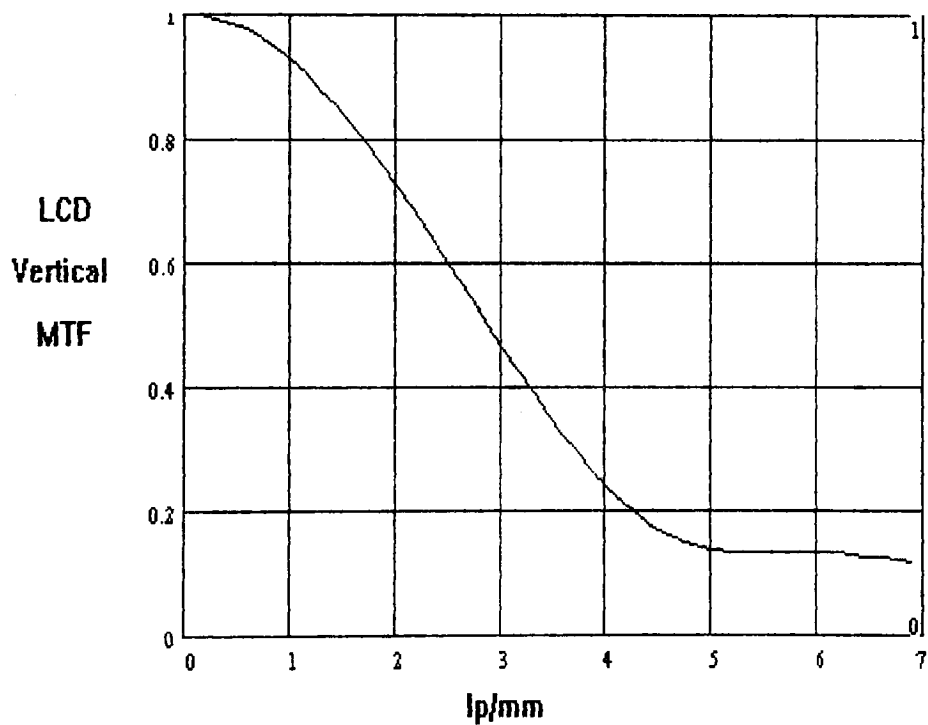


Figure 5-3 - Vertical MTF of SLM

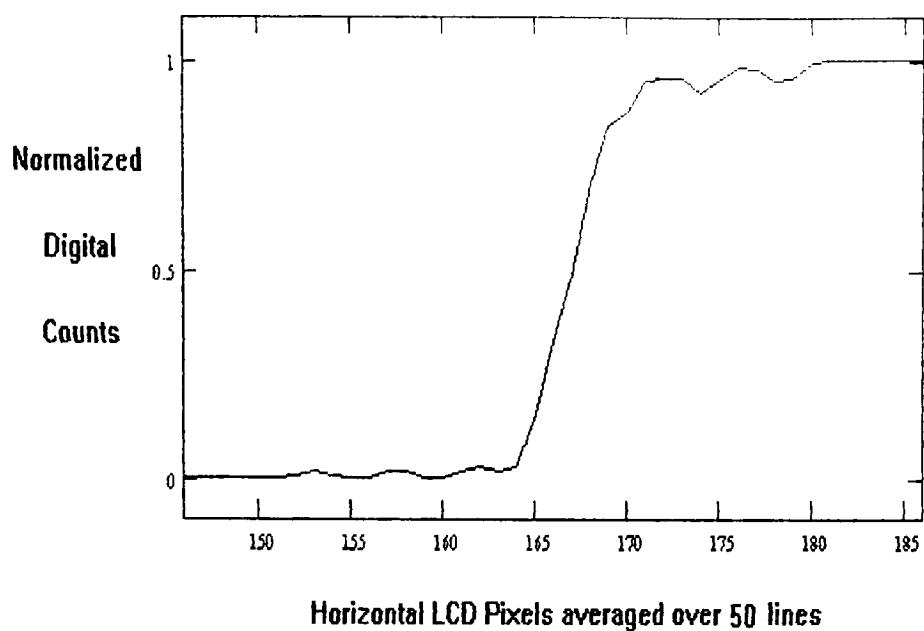


Figure 5-4 Normalized horizontal pixel values from figure 5-1.

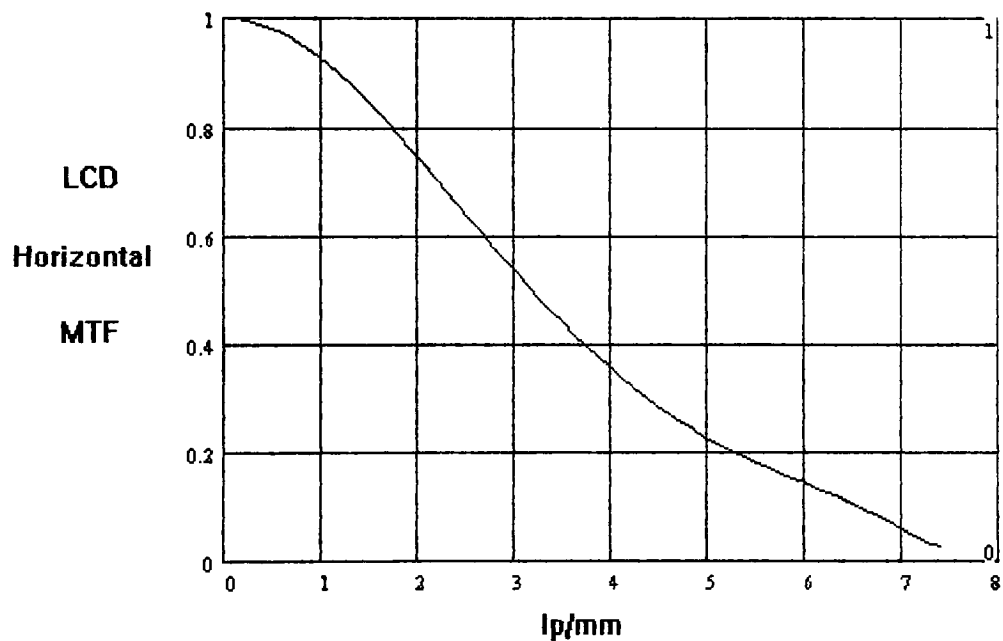


Figure 5-5 SLM horizontal MTF calculated from data at figure 5-4.

From figure 5-1 the non-continuous nature of the LCDs can be seen. It was found that having the LCD slightly out of focus minimized the higher frequency noise. The computed vertical MTF was better if calculated using data from the bottom of the "E" rather than the top. Data for the MTF graphs were taken from the middle of figure 1. A CCD camera was used to image the SLM. Several neutral density filters were used with the system setup to reduce the light to acceptable levels. Contrast measurements indicated that the LCD is not achromatic; the contrast varied by about 15% when the light was filtered through the different Epson TV filters. During initial testing of the components with a 150W white light source, a contrast ratio of 80:1 was found for the SLM.

It was also noted that after having the image of an "E" displayed for at least one hour, the LCD retained the image for about 15 minutes after it was no longer being applied. Furthermore, the contrast of the LCD was noticeably reduced after exposing one of the LCDs to high intensity white light without an intervening IR absorbing filter. The top line of the image appears to be fainter: this is probably due to the drive electronics.

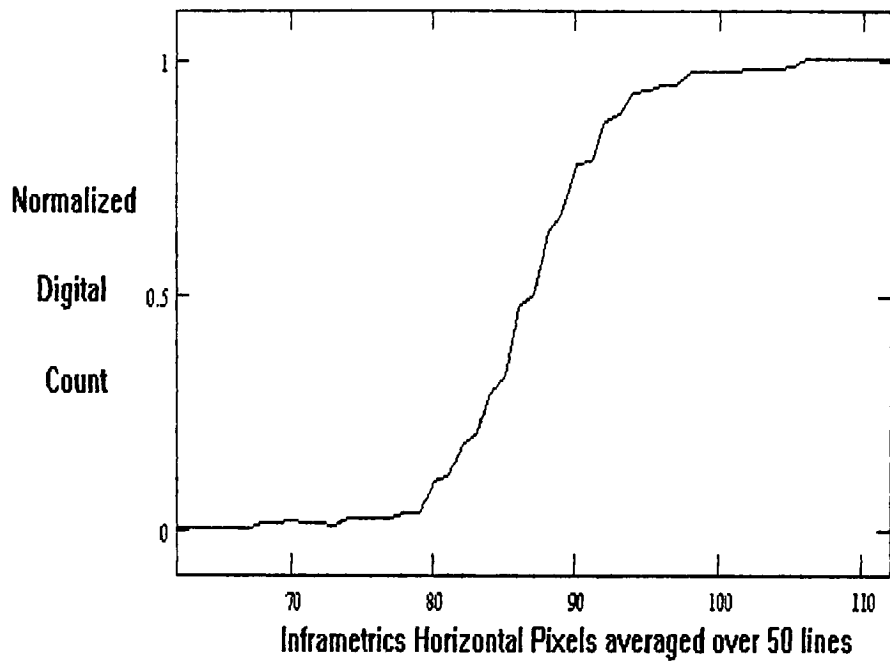


Figure 5-6 Horizontal pixels values for Inframetrics viewing system looking at a blackbody;

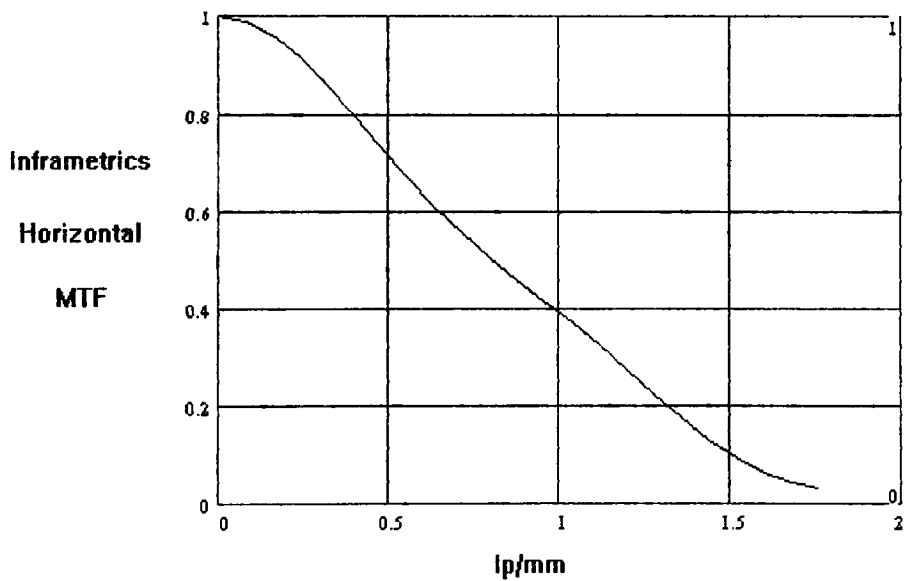


Figure 5-7 Inframetrics viewing system horizontal MTF from averaged data.

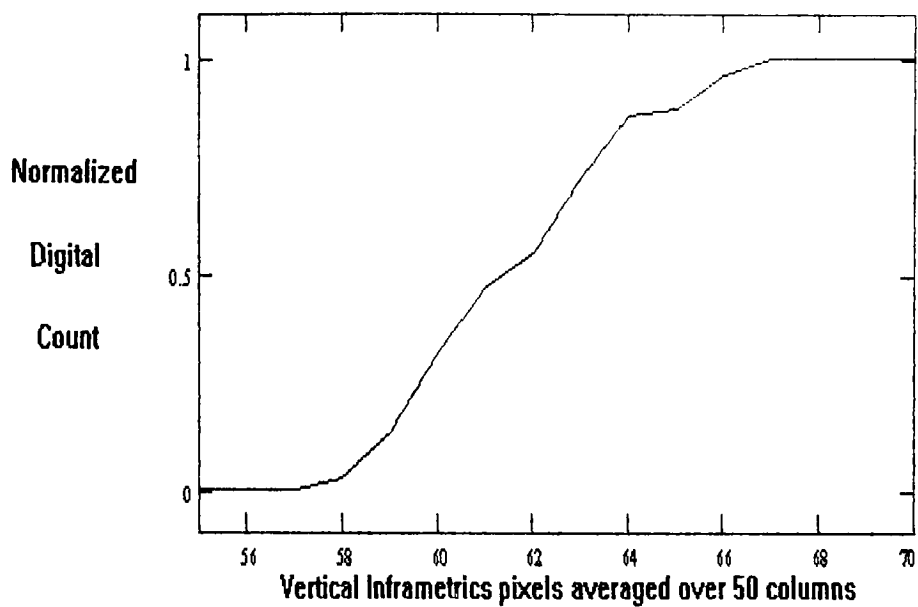


Figure 5-8 Vertical pixels from Inframetrics viewing a blackbody.

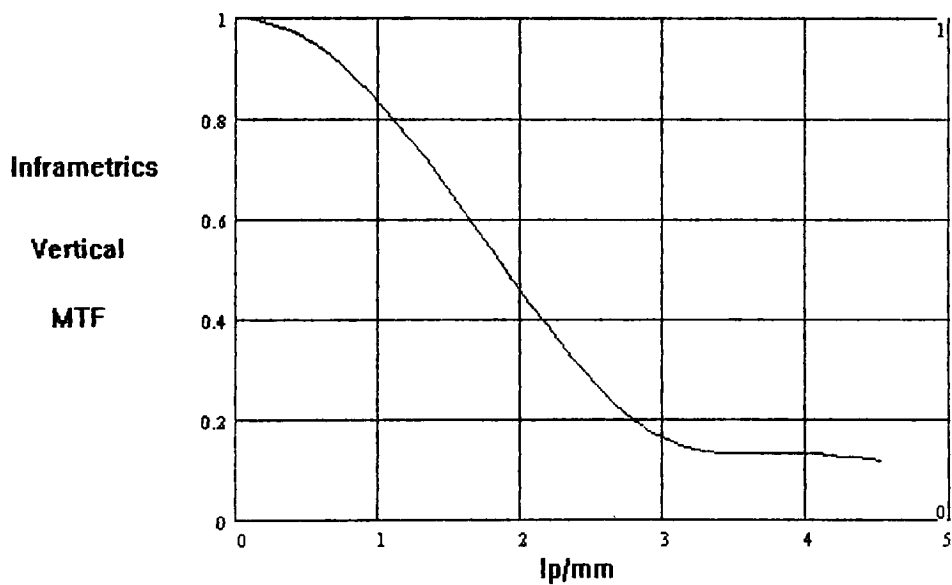


Figure 5-9 Inframetrics viewing system vertical MTF from averaged data.

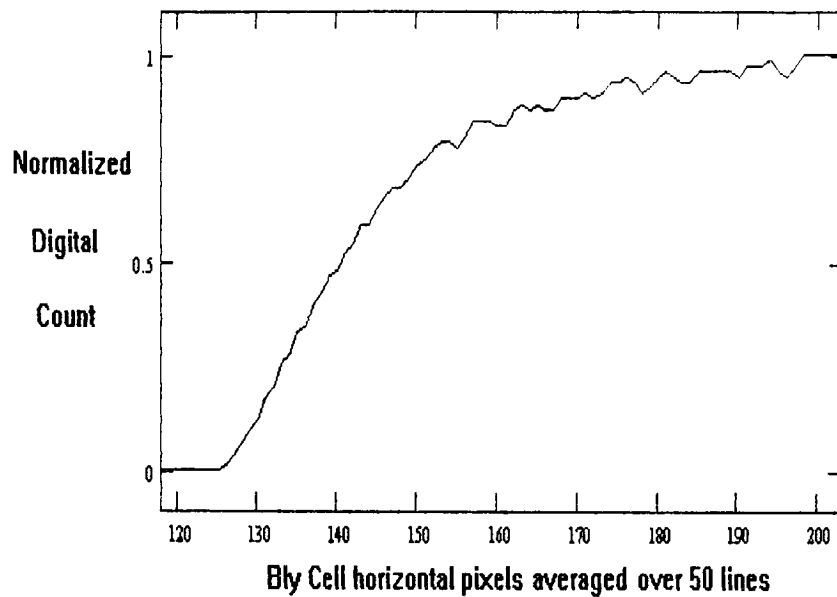


Figure 5-10 Horizontal pixel values from Bly cell illuminated by white light.

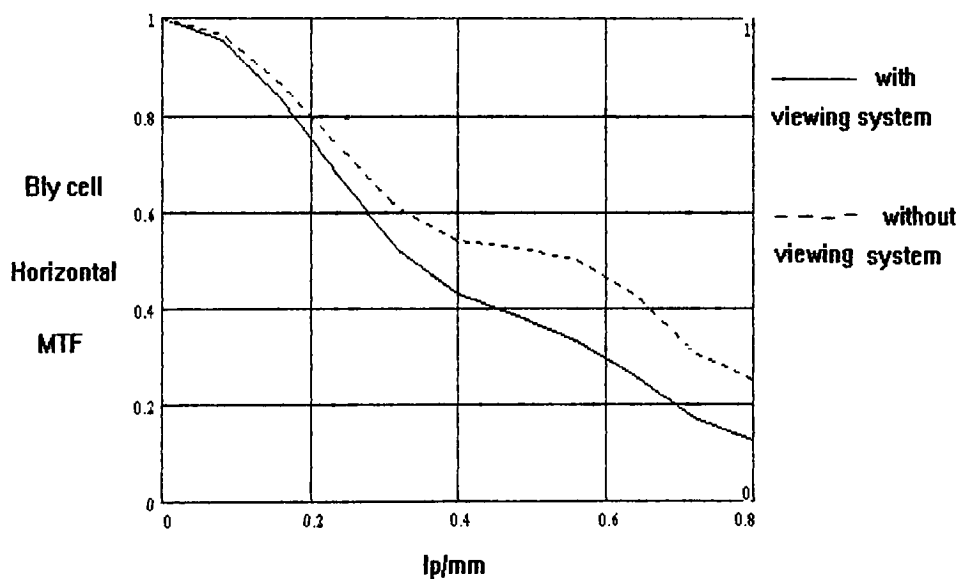


Figure 5-11 Horizontal MTF of Bly cell from averaged data with and without compensation for viewing system.

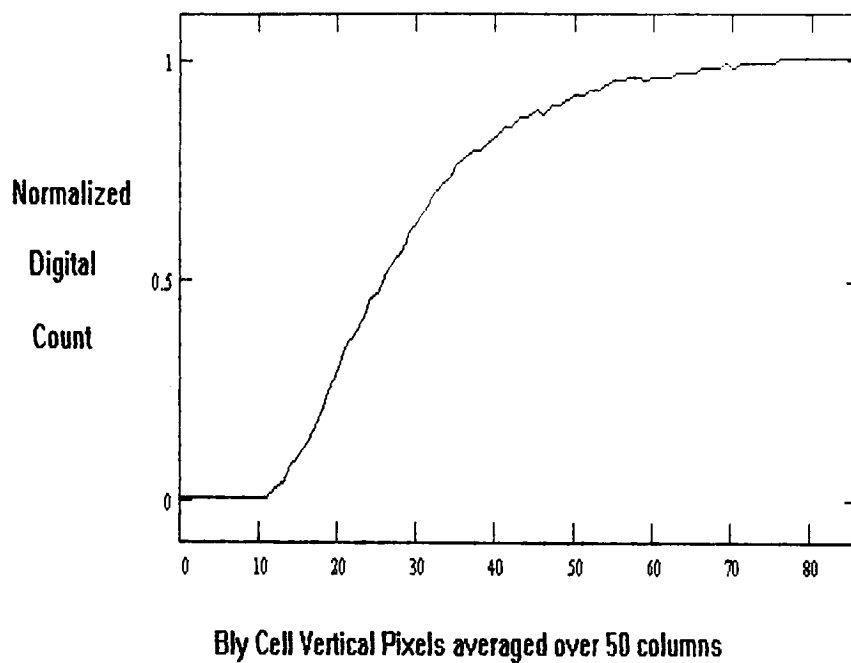


Figure 5-12 Vertical pixels values from Bly cell illuminated with white light.

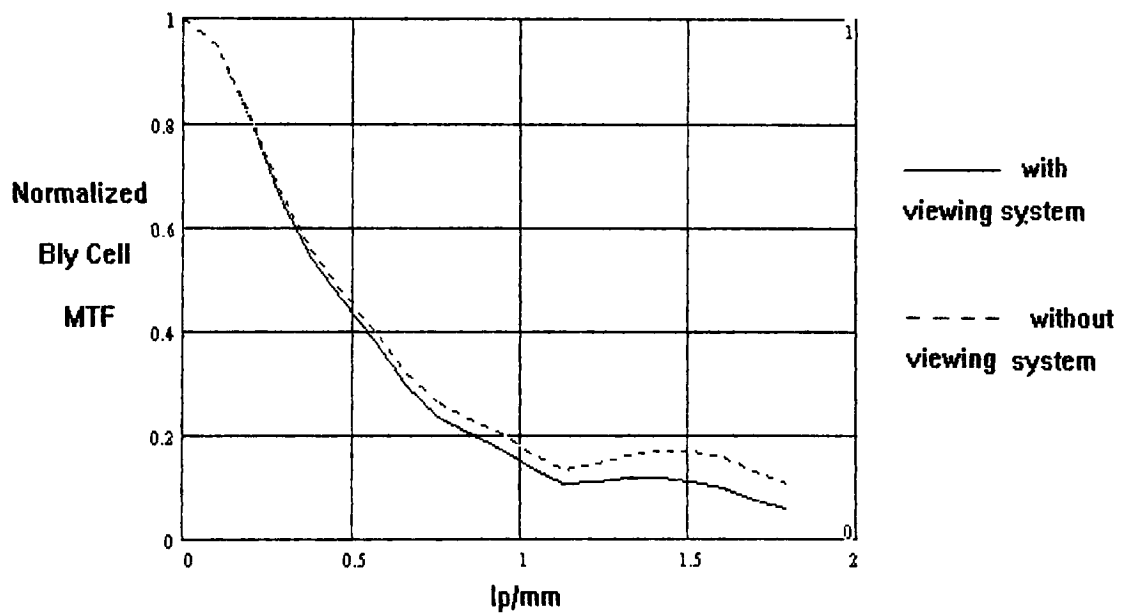
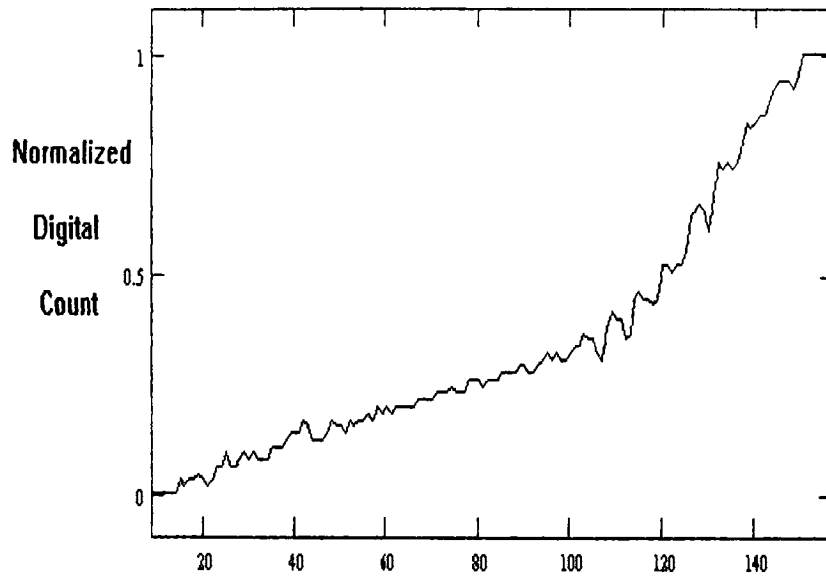


Figure 5-13 Vertical MTF of Bly cell from averaged data with and without compensation for viewing system.



System Horizontal pixels averaged over 50 lines

Figure 5-14 Horizontal pixels values from system.

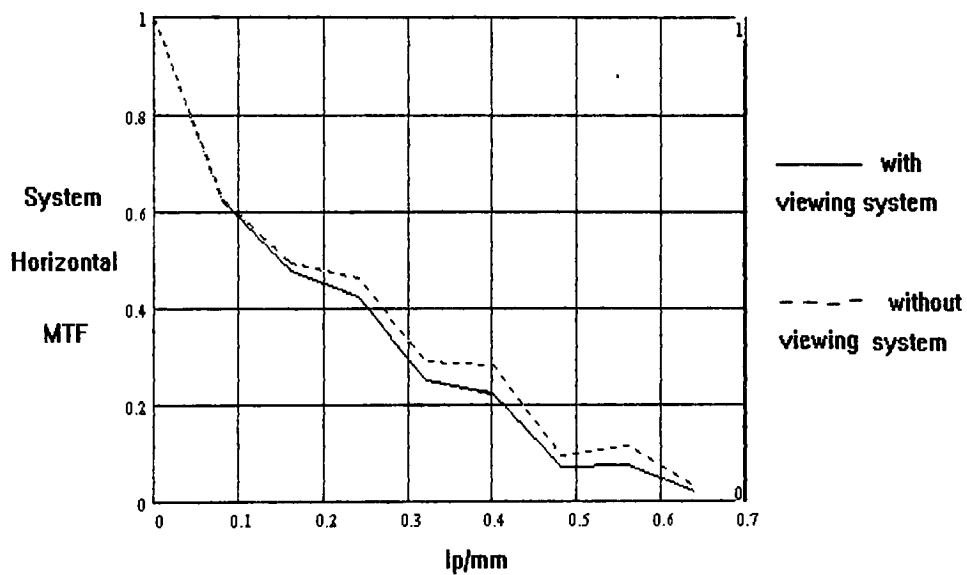


Figure 5-15 Horizontal MTF of system from averaged data with and without compensation for viewing system.

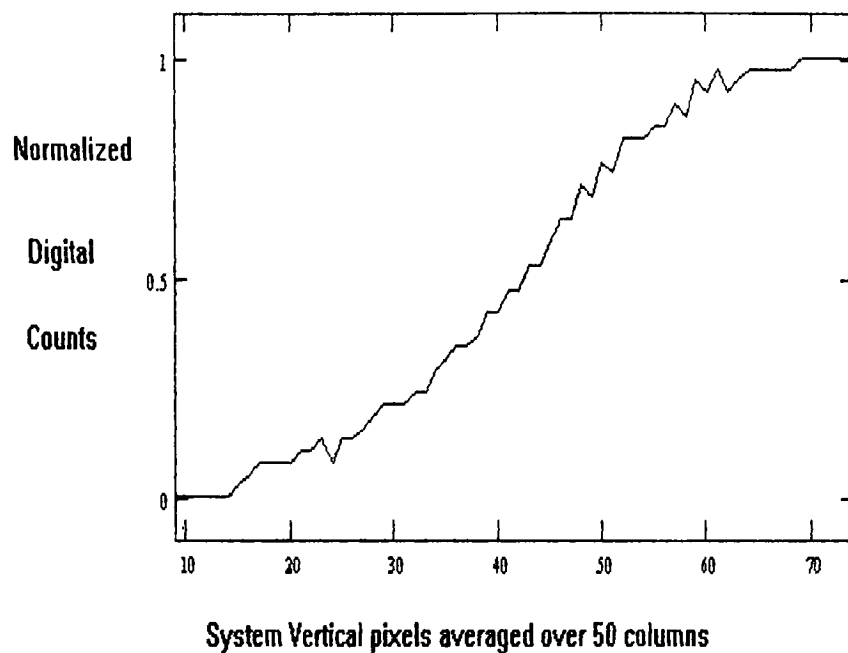


Figure 5-16 Vertical pixels values from system.

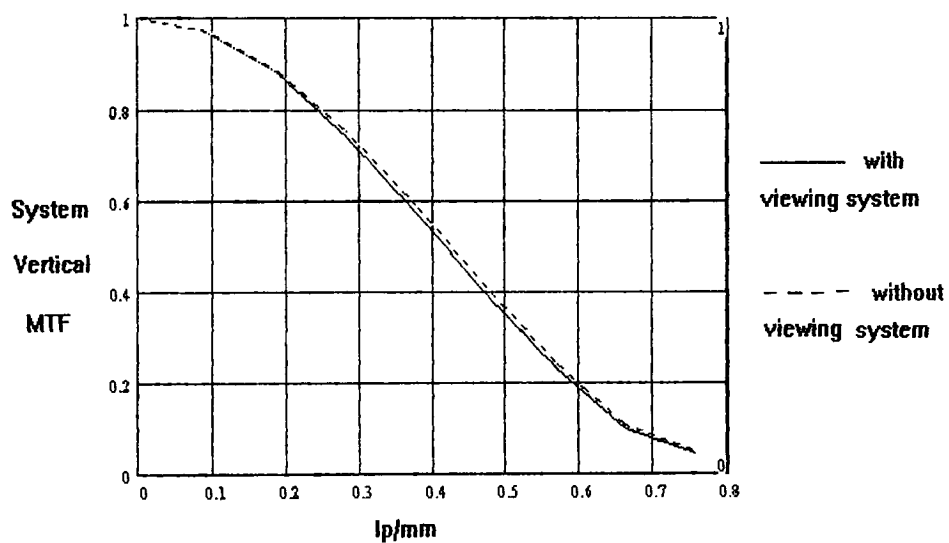


Figure 5-17 Vertical MTF of system from averaged data with and without compensation for viewing system.

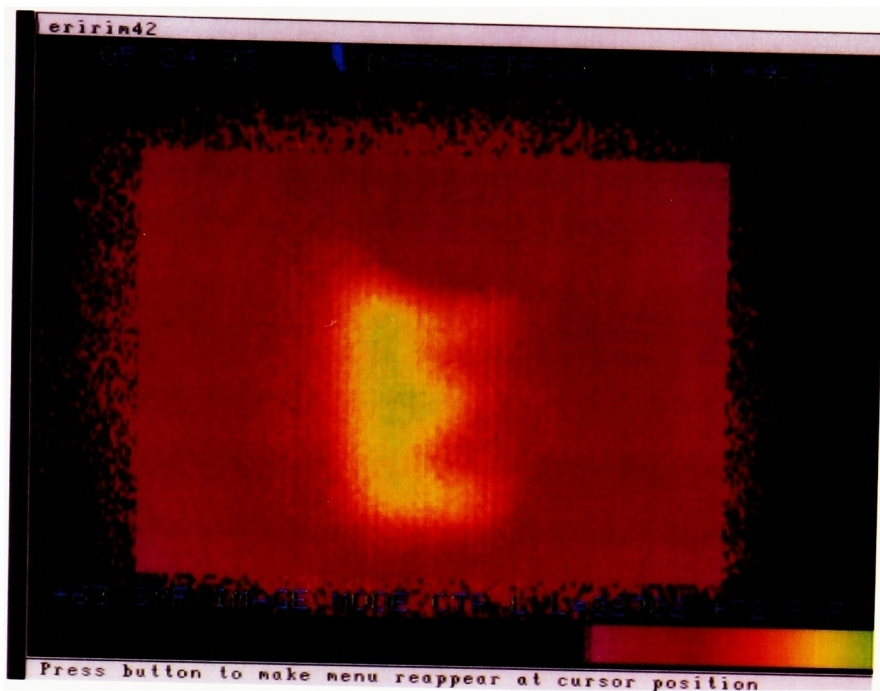


Figure 5-18 Pseudocolor IR image of an "E" projected through the system.

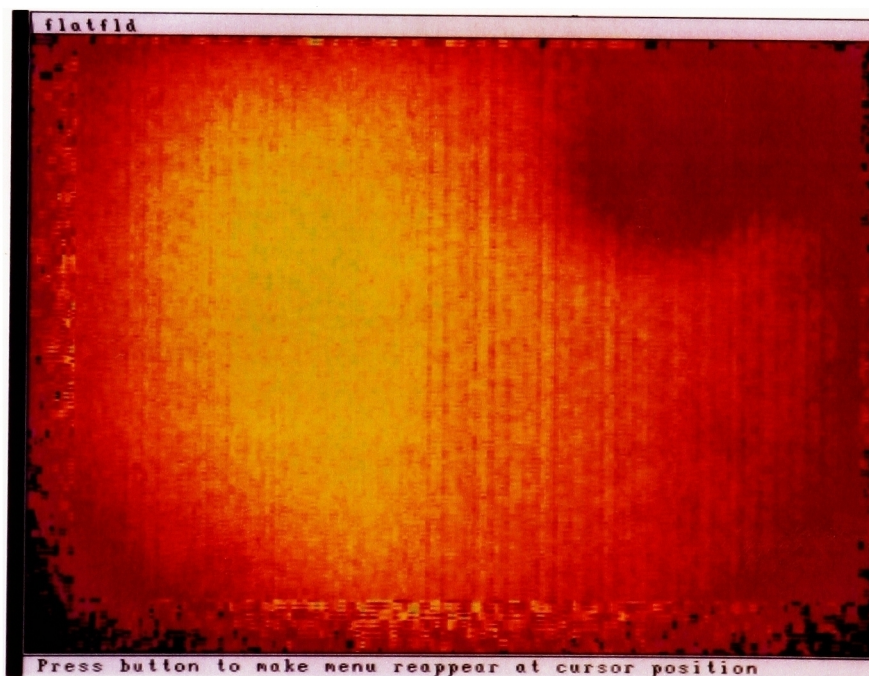


Figure 5-19 Pseudocolor image of a flat field.

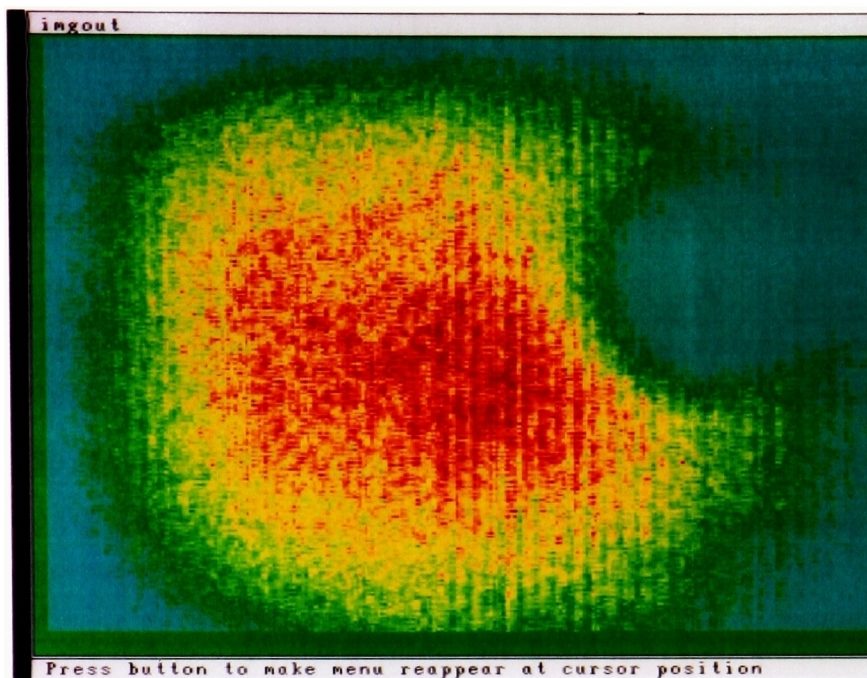


Figure 5-20 Pseudocolor image of the corrected input based on image at figure 5-19.

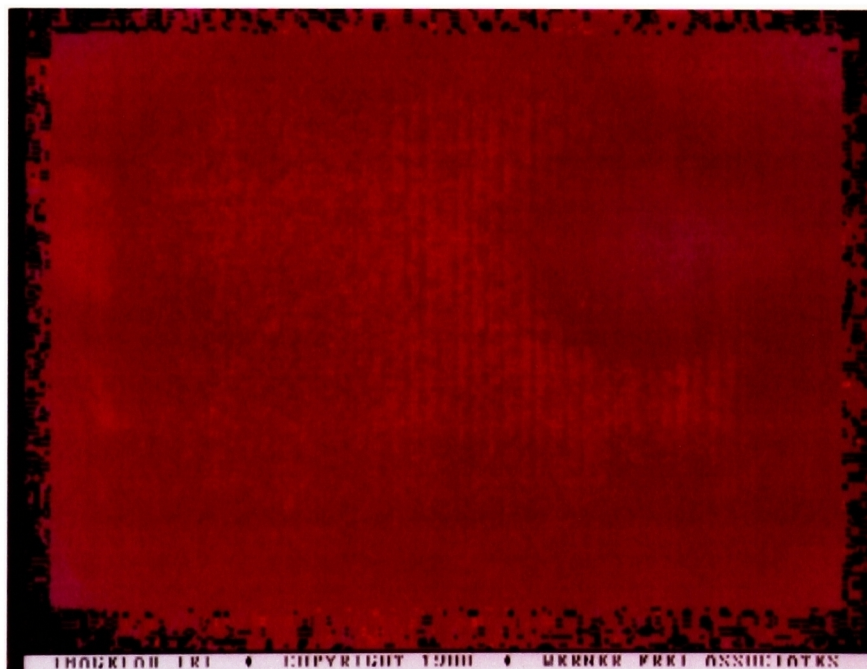


Figure 5-21 Pseudocolor IR image when figure 5-20 is the input to the system.

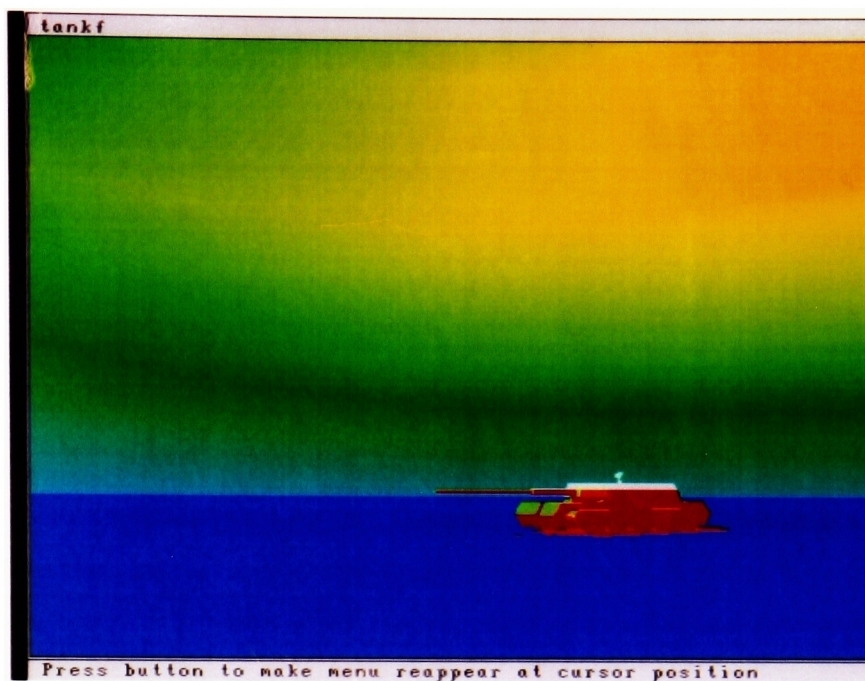


Figure 5-22 Pseudocolor image of an image used as input to the system.

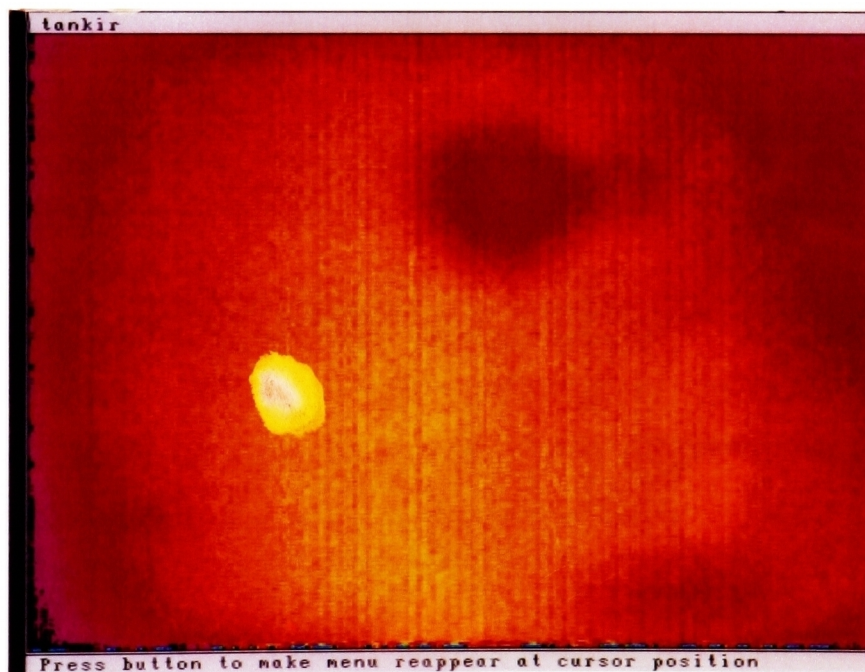


Figure 5-23 Pseudocolor IR image when figure 5-22 is input to the system.

5.2 Viewing system

The performance of the viewing system was quantified by using a blackbody source target. The data and MTFs are illustrated in figures 5-6 through 5-9. A wide slit was placed in front of the blackbody source to generate an edge. However, the MTF may actually be better because of the thermal conduction of the atmosphere. The camera was focused on an area the same size as the system image. The background noise was reduced when the camera was placed

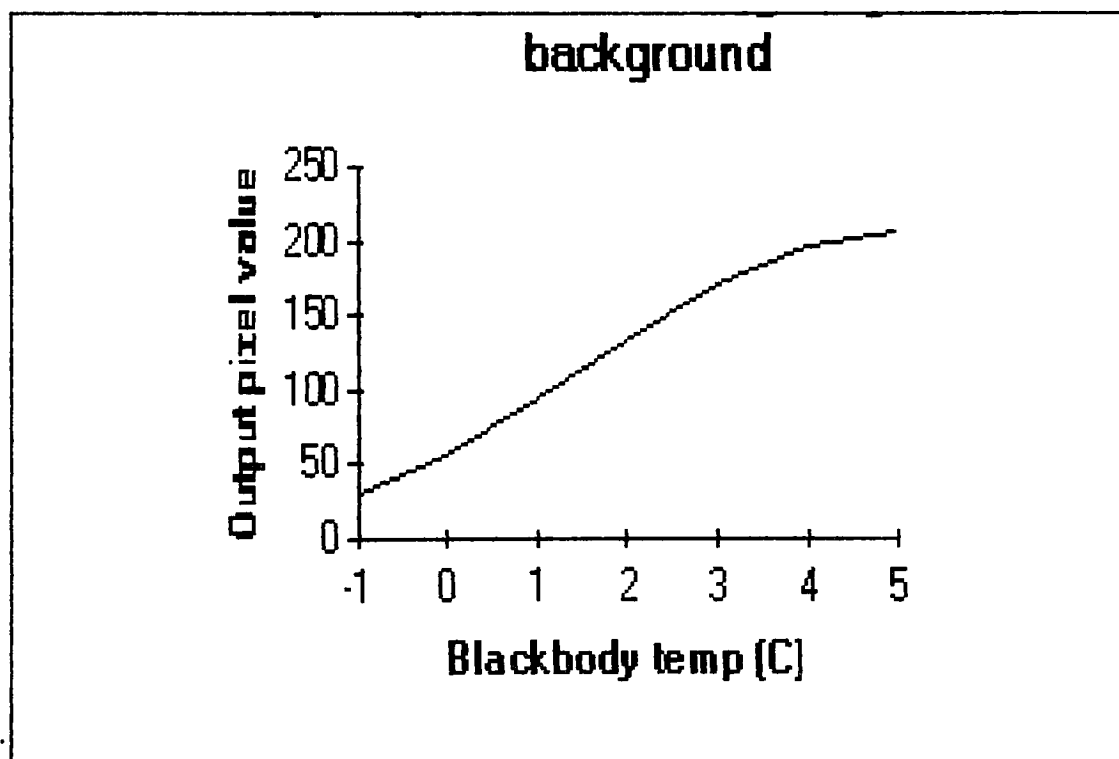


Figure 5-24 Calibration of the Inframetrics camera by using a variable blackbody source.

inside the freezer. Figure 5-28 illustrates the temperature to output pixel value of the Inframetrics systems set at the 5°C range.

5.3 Bly cell

The Bly cell data and MTFs are illustrated in figures 5-10 to 5-15. Notice how the tops of the pixel graphs are rounded off. This is probably due to thermal conduction by the air inside the cell. The Bly cell was pumped down to 5.5×10^{-6} Torr but could not hold this vacuum for very long.

5.4 System performance

The data and MTFs for the whole system are illustrated in figures 5-16 to 5-21. A bilevel image of the letter "E" which was used to generate the data in figures 5-16 to 5-21 is shown at figure 5-22. The system was adjusted to give the highest contrast. At first, it was thought that slight defocusing of the image might improve the MTF since it would blur the masked areas of the LCD. However; it was found that the final image was so blurred due to the low MTF that this was not necessary.

To correct for the radiometric variations across the image, a flat field of value 127 was applied to the LCD.

The resulting image is shown in figure 5-23. This image was then used in a program (appendix D) to compensate the input to correct for radiometric variations across the scene. The compensated image is illustrated at figure 5-24. The output with the compensated image as the input (figure 5-24) is shown at 5-25. Due to the limited dynamic range this was not attempted on an actual image.

The image generated when the figure 5-26 image was applied to the system is shown at 5-27. Note that 5-26 was a 512 by 512 image so that the first 20 and last 52 lines were not displayed. This accounts for the image of the tank appearing at the bottom of figure 5-26.

The dark circular area was caused by the reflection of the Inframetrics detector from its own lens, thus it could not be removed by changing the angle of view.

The problem of thermal conduction in the Bly cell was evident when imaging objects of different size. The greatest thermal contrast was obtained when flat fields were used. Even splitting the image into two equal areas of different grey values decreased the contrast between the two areas by about 25%.

The effect of lowering the temperature on the thermal contrast of the system is shown in figure 5-29. From this figure, the maximum number of usable grey levels is 40.

Using the data from figure 5-28 the maximum thermal contrast is 1.2°C.

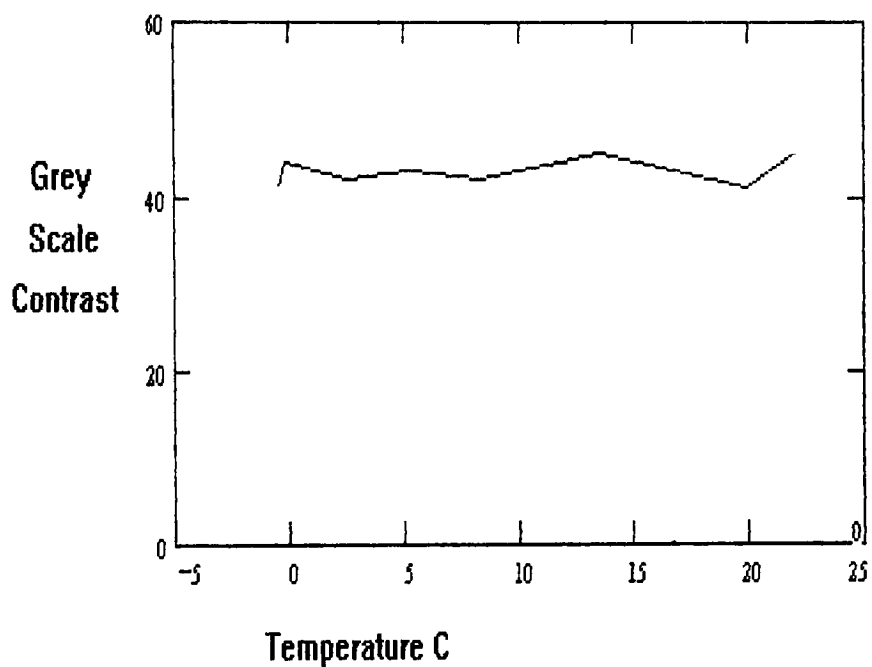


Figure 5-25 Effect of Bly cell ambient temperature on maximum contrast of system.

6.0 Conclusions and Recommendations

The results of the MTF and contrast measurements were significantly poorer than expected. Note that the MTF calculations assumed spatial invariance which was not true due to uneven illumination of the image. Uneven illumination can lower the frequency response of the system MTF (Chung and Hopkins, 1989). The frequency response of the system would restrict its application. Although some minor improvements could be made to the system, any significant improvements would require changes to the major subcomponents.

The system performance was limited for the following reasons:

- A. The light throughput could not be increased without damaging or destroying the IR blocking filter and/or SLM.
- B. The MTFs of the Bly cell and Inframetrics viewing system were limited by the small size of the image. The image could be easily enlarged by adjusting the distance between the components, however increasing the image size would decrease the already limited thermal contrast.
- C. The Bly cell was not operated at a vacuum which would maximize its resolution and conversion efficiency due to the limitations of the available vacuum pump.
- D. Although not investigated, the contrast of the Epson

LCD seems to have power limitations and be wavelength dependent. Other researchers have found that the contrast decreases with increased illumination. The contrast of the LCD changed by about 15% when different color filters were used.

D. The MTF of the LCD was limited due to the masking of the cells and the drive electronics. Furthermore, there was significant pixel variation across the LCD likely due to power distribution variations. The appearance of a ghost line above all horizontal lines and the combination of the overlap of successive fields limits the vertical MTF. The resampling of the input signal which could cause aliasing limits the horizontal MTF.

E. The noise in the images is a problem inherent in most far-IR detectors. By multiframe averaging the images, the noise was significantly reduced, but it also blurred the images.

F. As mentioned by Warnick (1990), the MTF of the Inframetrics is adversely affected by its diffraction limit, difficulty to focus, and the offset of the phasing of its two video fields. He also noted that the double resampling of the Inframetrics/Imaging Technologies viewing system decreases its MTF.

The thermal contrast of the system did not improve when the system was cooled as predicted by the equation in section 2. Using the equations in section 2.5, an improvement in the thermal contrast could not be expected unless the Bly cell was cooled over 40K degrees. At this ambient temperature the increase in the temperature range of the Bly cell is greater than the decrease in the grey level steps. It is not recommended that the Bly cell be cooled below -10°C ; an attempt to cool it to -17°C resulted in a rupture of the Bly cell.

An image grabbed at -2°C was more blurred than the same image grabbed at 23°C . This is attributed to the loss of vacuum from 5.5×10^{-6} to 10^{-4} torr in the Bly cell rather than to any differences in temperature.

The edge trace method of computing the MTF seemed to amplify the higher frequency noise excessively. Perron (1988) found that Tatian's method was accurate at low frequencies for a signal-to-noise ratio up to 30:1. However, considering that the IR images were very noisy, the use of another method for computing the MTF should be investigated.

To improve performance, the light throughput and contrast of the system must be improved. Currently the Bly cell has the worst MTF of all the subcomponents. The MTF of

the Inframetrics is only slightly better. The following steps could be taken to improve the system:

A. A setup similar to that used in the Epson TV projector could be implemented. In this setup the light source is split up into three primary colors, then each one is spatially modified by SLMs before being recombined. This would decrease the wavelength dependence of the SLMs while allowing more power through.

B. Using a larger newer LCD; A newer LCD would probably have higher contrast since the material in the cells would not be degraded. A larger LCD should be able to handle more power.

C. The resolution of the Bly could be improved by creating a harder vacuum and ensuring that the vacuum is maintained.

D. The drive electronics for the LCD could be replaced so that individual control over each pixel is possible. This should eliminate the ghost line above the SLM images.

Replacing the drive electronics would also avoid the possibility of aliasing in the horizontal direction.

Comparing the results with Warnick's (1990) work in the same area, he obtained a better system MTF, and a slightly better Bly cell MTF which is attributed to the harder vacuum. He does not have experimental results for his SLM. Warnick obtained a higher thermal contrast, while the

contrast of his SLM was only slightly worse than the Epson SLM. This is most likely due to the larger SLM. Other researchers have reported contrast ratios as high as 200 to 1 for the Epson LCD when using the device at lower power levels (Soutar *et al.*, 1993). By using a noncoherent light source, problems associated with the surface quality of the optics were not encountered. Otherwise, both systems would have problems handling the higher power necessary to generate a greater thermal contrast.

In summary, a system using a white light source is feasible, however; the system did not improve on previous results. Although the radiometric correction of the image by varying the image pixel values was shown to be feasible, it was not implemented due to the limited dynamic range. The problems associated with the drive electronics and overheating of the SLM should be addressed if further work is contemplated on this type of setup.

References:

B. Bates and P.C. Miller, "Liquid Crystal Television in Speckle Metrology", *Applied Optics*, 27, pp 2816-2817, 1988.

C.R. Batishko, R.A. Craig and K.A. Stahl, "An Infrared Simulator for Testing Electro-optical Systems Against Smoke and Obscurants", *Infrared Scene Simulation: Systems, Requirements, Calibration, Devices, and Modeling*, Milton Triplett, R. Barry Johnson, Editors, Proc. SPIE 940, pp. 157-165, 1988.

G.D. Boreman and E.R. Raudenbush, "Modulation Depth Characteristics of a Liquid Crystal Television Spatial Light Modulator," *Applied Optics*, 27, pp 2940-2943, 1988.

V.T. Bly, "Passive Visible to Infrared Transducer for Dynamic Infrared Image Simulation", *Optical Engineering*, 21, pp 1079-1082, 1982.

S.G. Burnay, T.L. Williams and C.H.N. Jones, *Applications of Thermal Imaging*, Adam Hilger, Bristol, 1988.

D. Casasent and Shoa-Feng Xia, "Phase correction of light modulators," *Optical Letters*, Vol 11, No 6, 1986.

Chang S. Chung and Harold H. Hopkins, "Influence of nonuniform amplitude on the optical transfer function," *Applied Optics*, Vol 28, No 6, pp 1244-1250, 1989.

Clark, K.J. Powell and M.K. Giles, "Using Liquid Crystal Devices as Input and Filter SLMs," SPIE Vol 1704 *Advances in Optical Information processing V*, 1992.

S.S. Cotariu, S.E. Monroe Jr. and J. Knopp, "A live input, live filter, liquid crystal correlator," SPIE Vol 1704 *Advances in Optical Information processing V*, 1992.

James E. Dillon, J. Schildraut and Kevin Silk, "A Tactical Infrared Scene Simulator Incorporating the Multiple Dynamic Simulator Infrared Emitter Array," *Characterization, Propagation, and Simulation of Infrared Scenes*, SPIE vol 1311, pp 320-325, 1992.

U. Efron, S.T. Wu, J. Grinberg and L.D. Hess, "Liquid-crystal based visible-to-infrared dynamic image converter," *Optical engineering*, Vol. 24, No 1, 1985.

Eppley Laboratories Inc., "Visible-to-IR Transducer prototype fabrication and performance data", (undated and unpublished).

James L. Foy, "IR CRT Scene Projector." Proceedings of the Fourth SDIO Scene Projection Workshop (SPW IV), AEDC-TR-92-1, pp 198-209, 1992.

J.D. Gaskill, Linear Systems, Fourier Transforms, and Optics, John Wiley & Sons, New York, 1978.

H. Gumbel, B. Jones Capone and R. Jones, "A discussion of infrared scene generators." *Characterization, Propagation, and Simulation of Infrared Scenes*, SPIE Vol 1311, pp 304-319, 1992.

L. Harris, R.T. McGinnes and B.M. Siegel, "The preparation and Optical Properties of Gold Blacks", *Journal of the Optical Society of America*, 38, 582-589, 1948.

L. Harris and J.K. Beasley, "The Infrared Properties of Gold Smoke Deposits", *Journal of the Optical Society of America*, 42, pp 134-140, 1952.

L. Harris and A. Loeb, "Conductance and Relaxation Time of Electrons in Gold Blacks from Transmission and Reflection Measurements in the Far Infrared", *Journal of the Optical Society of America*, 43, pp 1114-1118, 1953.

James L. Hester, "Thermal array target simulation technology/" *Infrared Scene Simulation Systems, Requirements, Calibration, Devices, and Modeling*, Milton Triplett, R. Barry Johnson, editors, SPIE Vol 940, 1988.

T.N. Horsky, G.J. Genetti, S.D. Lee, C.M. Schiller and C. Warde, "Deformable Membrane Mirror SLM for Projection of Dynamic IR scenes." Proceedings of the Fourth SDIO Scene Projection Workshop (SPW IV), AEDC-TR-92-1, pp 152-158, 1992.

K.D. Hughes, S.K. Rogers, J.P. Mills and M. Kabrisky, "Optical Preprocessing using Liquid Crystal Televisions", *Applied Optics*, 26, pp 1042-1044, 1987.

S. Jatamulia, G.M. Storti, W.M. Seiderman and J. Lindmayer, "Infrared signal processing using a liquid crystal television." *Optical Engineering*, Vol 30 No. 2. pp 179-182, 1991.

J. Killus, B. Elder, L. Siegel and M.B. Allweiss,
"Multiwavelength Scophony infrared scene projector."
*Characterization, Propagation, and Simulation of Infrared
Scenes*. SPIE Vol 1311, pp 327-339, 1992.

J.C. Kirsch, D.A. Gregory, M.W. Thie and B.K. Jones,
"Modulation characteristics of the Epson liquid crystal
television." *Optical Engineering*, Vol 31 No 5, pp 963-969,
1992.

S.P. Lake, A. Pritchard, I.M. Sturland, A.R. Murray, A.J.
Prescott and D.W. Gough, "Description and Performance of a
256x256 Electrically Heated Pixel IR Scene Generator."
Proceedings of the Fourth SDIO Scene Projection Workshop
(SPW IV), AEDC-TR-92-1, pp 166-172, 1992.

W. Lee and D.R. Snyder, "Flickerless Dynamic IR Scene
Generation for Simulation Applications", *Infrared Scene
Simulation: Systems, Requirements, Calibration, Devices, and
Modeling*, Milton Triplett, R. Barry Jongson, Editors, Proc.
SPIE 940, pp 176-181 1988.

T.M. Lillisand and R.W. Kieffer, *Remote Sensing and Image
Interpretation*, Hohn Wiley & Sons, New York, 1987.

H. Liu, J.A. Davis and R.A. Lilly, "Optical-data-processing
Properties of a Liquid-crystal Television Spatial Light
Modulator, *Optics Letters*, 10, pp 635-637, 1985.

H.S. Lowry, P.D. Elrod and T.C. Layne, "AEDC'S
Transportable Direct Write Scene Generation Test
Capability." Proceedings of the Fourth SDIO Scene Projection
Workshop (SPW IV), AEDC-TR-92-1, pp 141-150, 1992.

Scott B. Mobley, "Dynamic Infrared Scene Projection
Technology." *Characterization, Propagation, and Simulation
of Sources, and Backgrounds*, SPIE Vol 1486, pp 325-332,
1991.

S.K. Park, R. Schowengerdt and M. Kaczynski, "Modulation-
transfer-function Analysis for Sampled Image Systems",
Applied Optics, 23, pp 2572-2582, 1984.

J.S.L. Perron, "Comparison between edge tracing and slit
tracing in the measurement of the OTF." M.S. Thesis,
Rochester Institute of Technology, May, 1988.

A.P. Pritchard, "Dynamic IR scene generation: basic requirements and comparative display device design." *Infrared Scene Simulation Systems, Requirements, Calibration, Devices, and modelling*, Milton Triplett, R. Barry Johnson, editors, SPIE vol 940, pp 144-149, 1988.

A.P. Pritchard and S.P. Lake, "Electrically Heated Pixel (EHP) Arrays for Dynamic Infrared Scene Generation", *Infrared Scene Simulation: Systems, Requirements, Calibration, Devices, and Modeling*, Milton Triplett, R. Barry Johnson, Editors, Proc. SPIE 940, pp 182-188, 1988.

Don Pritchard and Burt Ludington, " NICS Infrared Halftone Technology." Proceedings of the Fourth SDIO Scene Projection Workshop (SPW IV). AEDC-TR-92-1, pp 159-164, February 1992.

W.H. Purdy and W.E. Woehl, "A Passive Thermal Screen for Infrared Scene Simulation," *Optical Engineering*, Vol 15 No 6, 1976.

B.E.A. Saleh and M.C. Teich, Fundamentals of Photonics, John Wiley & Sons Inc, New York, 1991.

F. Scott, R.M. Scott and R.V. Shack, "The use of Edge Gradients in Determining Modulation Transfer Functions", *Photographic Science and Engineering*, 7, pp 345-349, 1963.

C. Soutar, S.E. Monroe Jr. and J. Knopp, "Complex characterisation of the Epson Liquid crystal television," *Optical Pattern Recognition IV*, SPIE Conference 1959 Orlando, 1993.

M.A. Spivak, "Parylene Thin Films for Radiation Applications", *Review of Scientific Instruments*, 41, pp 1614-1616, 1970.

Donald R. Stauffer and Barry I. Cole, "Thermal scene projectors using microemitters." *Optical Engineering*. Vol 30 No. 11, 1991.

Andrei Szilagyi, Gregory Um, Yeon H. Lee, David E. Foley and Mois A. Navon, "Actuated Mirror Array technology." Proceedings of the Fourth SDIO Scene Projection Workshop (SPW IV), AEDC-TR-92-1, pp 174-184, 1992.

A.M. Tai, "Low-cost LCD Spatial Light Modulator with High Optical Quality, *Applied Optics*, 25, pp 1380-1382, 1986.

B. Tatian, "Method for Obtaining the Transfer Function from the Edge Response Function", *Journal of the Optical Society of America*, 55, pp 1014-1019, 1965.

J.S. Warnick, "A QUANTITATIVE ANALYSIS OF A SELF-EMITTING THERMAL IR SCENE SIMULATION SYSTEM." M.S. Thesis, Rochester Institute of Technology, April 1990.

J.S. Warnick, E. Shor and J.R. Schott, "THERMAL INFRARED SCENE SIMULATION," Final Report #RIT/DIRS 89/90-51-133, January 1990.

C.S. Williams and O.A. Becklund, Introduction to the Optical Transfer Function, Wiley-Interscience, New York, 1989.

William L. Wolfe and George J. Zissis, editors, The Infrared Handbook, Environmental Research Institute of Michigan, 3rd ed., 1989.

Ludwig G. Wolfert, "Dynamic Scene Projection in the UV to IR Spectra with Cathode Ray Tube Technology." Proceedings of the Fourth SDIO Scene Projection Workshop (SPW IV), AEDC-TR-92-1, pp 211-216, 1992.

Hon-sun Wong, "Effect of knife-edge skew on modulation transfer function measurements of charge-coupled device imagers employing a scanning knife edge." *Optical Engineering*, vol 30, No. 9, 1991.

R.L. Woltz, "The SCANAGON, a Dynamic Scene Projector", *Infrared Scene Simulation: Systems, Requirements, Calibration, Devices, and Modeling*, Milton Triplett, R. Barry Johnston, Editors, Proc. SPIE 940, pp. 171-175, 1988.

F.T.S. Yu, S. Jutamulia and X.L. Huang, "Experimental Application of Low-cost Liquid Crystal TV to White-light Optical Signal Processing", *Applied Optics*, 25, pp 3324-3325, 1986.

F.E. Zissis, "Fundamentals of infrared: a review", Selected Papers on Radiometry, reprinted from SPIE Proceedings 1975, Irving J. Spiro and Brian J. Thompson Editors, SPIE Optical Engineering Press, 14, 1990.

Appendix A

Spatial Light Modulator

Manufacturer	Epson
Model	Crystal Image video projector
Resolution	6.3 lp/mm
Visibility	.98
LCD Size	2.54 x 1.9 cm
Speed	60 Hz
cell size	55 x 60 μm
center to center spacing	80 x 90 μm
pixel count per LCD	320 x 220
active area	46%
transmission efficiency ($\lambda = .6328$)	about 43%
optical flatness	.5 λ to 4 λ
Update rate	60 Hz

Appendix B
Specifications of VIRT

Manufacturer	Eppley Laboratory, Inc.
Model	C1933
Membrane Absorbtion	61%
Operating vacuum	$< 10^{-3}$ Torr
Window material	Pyrex (front) Germanium (rear)
Cell Material	cellulose nitrate film 450-500Å thick supports a goldblack deposit
MTF at 3 cycles/mm	50%
Maximum temperature	70°C
Time constant	< 25 msec
Dimensions	Outside diameter: 6" thickness 1 9/16"

ΔT of 25° for illumination of approximately 30 lumens

Appendix C
Specifications of Inframetrics Camera

IR Camera	Model 600
Spectral Bandpass	8 - 12 μm
Detector Type	HgCdTe (LN ₂ cooled)
Field of View	15 deg Vertical by 20 degree Horizontal
Resolution	2 mRad - 148 IFOV's Horizontal, 256 Pixels/Line 2 mRad - 130 IFOV's Vertical, 200 lines/frame
Output Format	RS-170, NTSC
Dynamic Range	7 bit, 128 levels, 42 dB 8 bit, 256 levels (48db) with Image Averager
NE Δ T (typical 8-12 μm)	@30°C less than 0.2°C @30°C with image averager; < 0.05°C
Temperature Measurement Range	-20 to +400°C Normal range 0 to +1000°C Extended Range
Temperature Readout Resolution	3 digits
Ambient Operating Temperature	-15 to +45°C

Appendix D

Program to extract sampled data to allow horizontal MTF calculation by using Tatians method re Journal of Optical society of America, V 55, No 8 1965, implemented in Mathcad Program written in Borland C++ Ver 2.0 by G. Ralph, 1993.

```
#include <stdio.h>
#include <stdlib.h>
#include <fstream.h>

// Global variables

#define MAXH 512 // number of pixel in line
#define Start 150 // start at this horizontal location
#define startln 150 // get data from this line
#define lines 50 // define number of lines to average
over

main()
{
    int i,j;
    long int k;
    unsigned char DataH[MAXH/2][lines];
    unsigned char I;
    FILE *fpin;
    fpin = fopen("c:\\horzbo40.img","rb");
    if (!fpin) {
        cerr << " \n error opening read file";
    }
    else {
        for (i = 0; i < startln; i++){
            for ( j = 0; j < MAXH; j++) {
                I = fgetc(fpin); // discard data until reach
                desired line
            }
        }

        for(i=0; i < lines; i++){
            for ( j = 0; j < MAXH; j++) {
                if ( (j >= Start) && (j < (Start + 256))) {
                    DataH[j-Start][i] = fgetc(fpin);
                }
                else { I = fgetc(fpin); }
            }
        }
        cout << " \n file read";
        fcloseall();

        for(j=0; j < 256; j++){
            k = 0;
            for( i = 0; i < lines; i++){ // average lines
                k = DataH[j][i] + k;
            }
        }
    }
}
```

```

        }
        DataH[j][2] = (int)k/lines;
    }

    ofstream fpout("c:\\htst3.mtf",ios::out);
    if (!fpout){
        cerr << " unable to open file for output";
    }
    else {
        cout << " /n outputting file /n";
        for (j = 0; j < 256; j++){
            cout << " " << (int)DataH[j][0] << " " <<
            (int)DataH[j][2] << " " << (int)DataH[j][lines];
            fpout << " " << int(DataH[j][2]);
        }
        fpout.close();
        cout << " /n all done";
    }
    }
    return(0);
}

```


Appendix D

Program to extract sampled data from array for vertical MTF calculation also averages data over a specified number of points. Using Taitians method re Journal of Optical society of America, V 55, No 8 1965. MTF calculations done via MATHCAD. Program written in Borland C++ Ver 2.0 by G. Ralph, 1993.

```
#include <stdio.h>
#include <stdlib.h>
#include <fstream.h>

// Global variables

#define MAXH 512
#define Start 50
#define line 240
#define num 50 // number of lines to average

main()
{
    int i,j;
    unsigned char Data[MAXH/2][num];
    long int k;
    char I;
    FILE *fpin;

    fpin=fopen("c:\\lcdmtf98.img","rb");
    if (!fpin) {
        cerr << " \n error opening read file";
    }
    else {
        for (i = 0; i < Start; i++){
            for ( j = 0; j < MAXH; j++) {
                I=fgetc(fpin); // discard lines until reach
desired line
            }
        }

        for ( i = Start; i < (Start + 256); i++){
            for ( j = 0; j < MAXH; j++) {
                if( (j >= line) && (j < (line + num))) {
                    Data[i-Start][j - line] = fgetc(fpin);
                }
                else { I = fgetc(fpin); }
            }
        }
        cout << " \n file read";
        fcloseall();
    }
}
```

```

    for ( i = 0; i < 256; i++){
        k = 0;
        for ( j = 0; j < num; j++) {
            k = Data[i][j] + k;
        }
        Data[i][2] = (int)k/num;
    }

    ofstream fpout("c:\\vlcd3.mtf",ios::out);
    if (!fpout){
        cerr << " unable to open file for output";
    }
    else {
        for (i = 0; i < 256; i++){
            fpout << " " << int(Data[i][2]);
            cout << " " << int(Data[i][0]) << " " <<
int(Data[i][2]) << " " << int(Data[i][num]);
        }
        fpout.close();
        cout << "  \n  all done";
    }
}
return(0);
}

```

Appendix D

Program to modify an input image to compensate for the spatially dependent variations across the image. Program written in Borland C++ Ver 2.0 by G. Ralph, 1993.

```
#include <stdio.h>
#include <stdlib.h>
#include <fstream.h>
#include <math.h>

// Global variables

#define MAXH 512          // max numnber of horizontal pixels
#define MAXV 480          // max number of vertical pixels
#define Vert 20          // start of displayed vertical image
area
#define Horz 10          // start of displayed horizontal image
area
#define startV Vert
#define EndV MAXV - Vert
#define startH Horz
#define EndH MAXH - Horz

unsigned char Xform(unsigned char J,int Z); // quadratic
linear conversion

main()
{
int i,j,l,H,W, header,hdr2, Dif,startleft, starttop,
bottomend, endright;
int m, zval;
float HA, WA;
long avg,k;
unsigned char I,J, flatfld[MAXH], image[MAXH];
header = 0;
hdr2 = 0;
FILE *fpin, *fpimg, *fpout;

// get input from user about images

cout << "\n input left coordinates of field:";
scanf( "%d", &startleft);
cout << "\n enter top coordinate: ";
scanf("%d",&starttop);
cout << " \n \n \n enter bottom coordinates of field: ";
scanf("%d",&bottomend);
cout << " \n enter right coordinates of field: ";
scanf("%d",&endright);
cout << " \n enter o/p for an I/P of zero:  ";
```

```

scanf("%d",&zval);
cout << " \n \r enter number of bytes in header of image to
be displayed: ";
scanf("%d",&header);

fpin = fopen("c:\\flatfld.img","rb");
if (!fpin){
    cerr << "error opening input file \n "; }
else {
    for ( i = 0; i < hdr2; i++){ // usually no header
        I = fgetc(fpin); // overloaded operators skip
control chars
    } // ignore header
    for (i = 0; i < starttop; i++){
        for ( j = 0; j < MAXH; j++) {
            I = fgetc(fpin); // ignore beginning of
file data
        }
    }

    avg = 0; // find avg of flat field
    k = 0;
    for ( i = starttop; i < bottomend; i++) {
        for ( j = 0; j < MAXH; j++){
            I = fgetc(fpin); // go to start of data
collection
            if((startleft <= j) && (j <= endright)){
                avg = int(I) + avg;
                k = k + 1;
            }
        }
    }

    avg = avg/k;
    I = avg;
    cout << avg << " " << I;
    avg = Xform(I, zval);
    cout << " avg found: " << hex << avg << " (hex) \n";
    fcloseall();

    // CORRECT INPUT IMAGE FOR SPATIALLY DEPENDENT
DIFFERENCES ACROSS
    // IMAGE PLANE BY USING FLAT FIELD IMAGE AS A BASELINE
    // PROGRAM ASSUMES THAT IMAGE LOCATION WILL NOT
CHANGED!!!!

    // Open files

    fpin = fopen("c:\\flatfld.img", "rb");
    fpimg= fopen("c:\\image.img", "rb");
    if (!fpin && !fpimg) {

```

```

    cerr << "\n \r cannot open input file(s) \n"; }
else {
    fpout = fopen("C:\\dtst.img", "w+b");
    if(!fpout) {
        cerr << " /n error opening output file /n "; }
    else {
        for( i=0; i < header; i++){    // ignore header info
            J = fgetc(fpimg);
            fprintf(fpout, "%c",J);
        }
        for ( i = 0; i < Vert; i ++ ) {
            for(j = 0; j < MAXH; j++){
                // don't change pixels which are not
                J = fgetc(fpimg);    // part of image displayed
                fprintf(fpout, "%c",J);
            }
            for ( k = 0; k < starttop; k ++ ) {
                for(l = 0; l < MAXH; l++){
                    I = fgetc(fpin);    // go to top of flat field
image
                }
            }

            // compensate for different image sizes, get pixel
values, and
            // correct image to be displayed

            H = bottomend - starttop;
            W = endright - startleft;
            HA = (float)(EndV-Vert)/(float)H;    // vertical ratio
of image pixels to flat field
            WA = (float)(EndH - Horz)/(float)W;    // ratio of
horizontal pixels
            k=0;

            // get one horizontal line from flat field image
            for (l = 0; l < MAXH; l++) {
                flatfld[l] = fgetc(fpin);
                if((int)flatfld[l] < zval) flatfld[l] = (char)zval;
                if((int)flatfld[l] > zval + 48) flatfld[l] =
(char)(zval + 48);
            }

            for (i = Vert; i < EndV; i++){

                // vertical alignment
                for (j = 0; j < MAXH; j++) {    // get one line from
image
                    image[j] = fgetc(fpimg);

```

```

    }
    if( (i-startV) > HA*(k+1)){ // get another line from
flat field
        for (l = 0; l < MAXH; l++) {
            flatfld[l] = fgetc(fpin);
            if((int)flatfld[l] < zval){ flatfld[l] =
(char)zval; }
            if((int)flatfld[l] > zval + 48){ flatfld[l] =
(char)(zval + 48);}
        }
        k = k + 1;
        cout << k << " ";
    }
// now for some horizontal pixel hocus pocus

    l = 0;
    for( j= 0; j < startH; j++) {
        J=image[j];
        fprintf(fpout, "%c",J);
        for ( j = startH; j < EndH; j++){
            if( (j-startH) <= WA*(l + 1)){ // correct pixel
values
                I = Xform(flatfld[l+startleft],zval); // convert
flat field
                m = (int)image[j] + avg - (int)I; // correct for
radiometry
            }
            else { // get next flat field pixel
                l = l + 1;
                I = Xform(flatfld[l+startleft],zval); // convert
flat field
                m = (int)image[j] + avg - (int)I; // correct for
radiometry
            }
            if( m < 0){ //check if number too low
                m = 0; // if yes, set to smallest possible
number
            }
            if ( m > 255) { // check if too high
                m = 255; // if yes, set to highest possible
number
            }
            J = (char)m;
            fprintf(fpout, "%c",J);
        }
        for ( j = EndH; j < MAXH; j++){
            J = image[j];
            fprintf(fpout, "%c",J);
        }
    }
    for (i = EndV; i < MAXV; i++){

```

```

        for (j = 0; j < MAXH; j++) {
            J = fgetc(fpimg);
            fprintf(fpout, "%c",J); // output rest of image
        }
        cout << "\n field done";
        fcloseall();
        cout << " \n \n All's WELL \a \r \r";
    }
}
return(0);
}

// subroutine to convert pixel value from a quadratic curve
// to a linear
// line

unsigned char Xform(unsigned char X1, int C1) {

double A1,B1, SQ;
unsigned char Xs;
int y,x;

A1 = -.0007653; // define quadratic constants
B1 = 0.385; //
// constants found by linear regression
y = int(X1);

    SQ = B1 * B1 - (4 * A1 * (C1 - y));
    if ( SQ < 0) {
        x = 0; // -ve only if y less than C1
    }
    else {
        SQ = pow(SQ,.5);
        x = (-B1 + SQ)/(2 * A1);
        if( (x < 0) || (x > 255)){
            x = (-B1 - SQ)/(2*A1);
            if ( x < 0) {
                cout << "\n \r quadratic number out of
bounds" << dec << y << " " << x;
                x = 0;
            }
            if ( x > 255) {
                cout << "\n \r quadratic number out of
bounds" << y << " " << x;
                x = 255;
            }
        }
    }
    Xs = char(x);
}

```

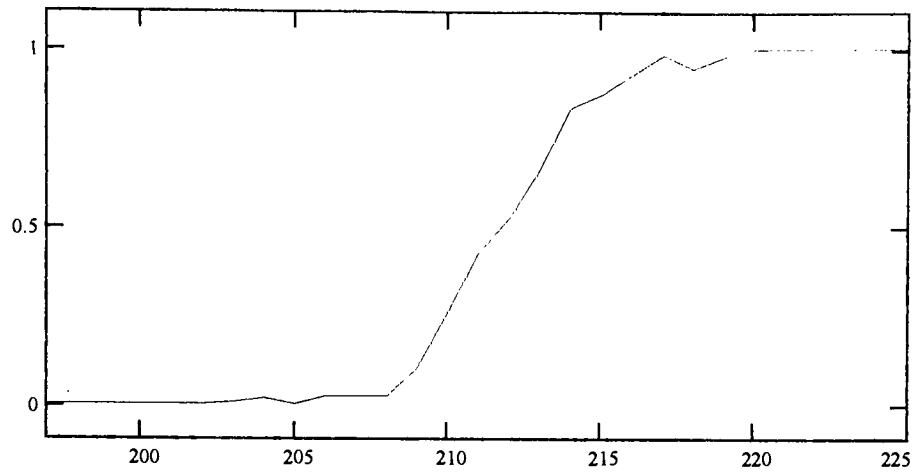
```
return(Xs);  
}
```


Example of Taitian's method of calculating OTF n = 0..255

```

N 256      Nq      N      j  0..255      ARyj  READ( lcdvert )      ARyii  ARyii
                                o  0..a  p  b..255      a  202      b  220
                                Aryo  Arya  Aryp  Aryb
mn := min( Ary )      mx  max( Ary )
mn = 34
                                input data
                                Aryii  mn /
                                ( mx  mn )

```



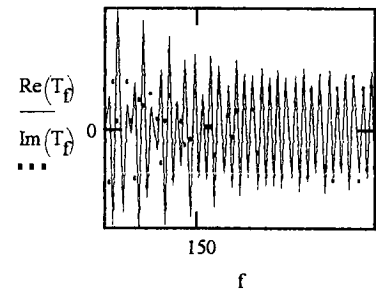
$$f := Nq..Nq + 64$$

$$k_f := \pi \cdot \frac{f - Nq}{N} \quad \text{psi}_n := n - Nq$$

$$T_f := \sum_n \left(Ary_n \cdot \exp \left(-2i \cdot \frac{f - Nq}{N} \cdot \pi \cdot \text{psi}_n \right) \cdot 2i \cdot \frac{f - Nq}{N} \cdot \pi \right)$$

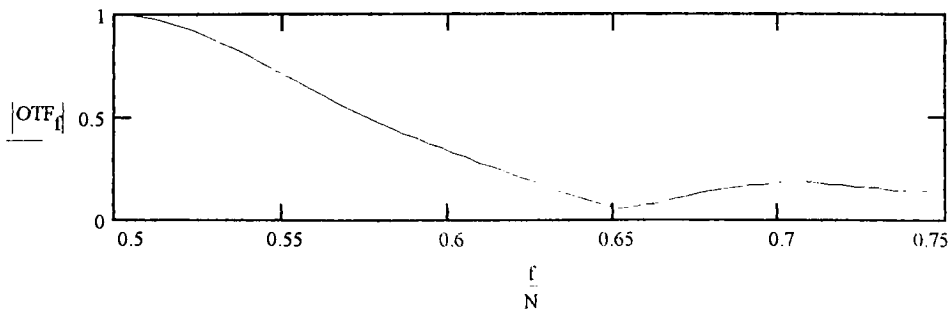
$$C_f := \frac{\cos \left[(Nq + .5) \cdot 2 \cdot \frac{f - Nq}{N} \cdot \pi \right] \cdot \pi \cdot \frac{f - Nq}{N} \cdot 2}{\sin \left(\pi \cdot \frac{f - Nq}{N} \right) \cdot 2}$$

$$S_f := \frac{\sin \left[(Nq + .5) \cdot 2 \cdot \frac{f - Nq}{N} \cdot \pi \right] \cdot \pi \cdot \frac{f - Nq}{N} \cdot 2i}{\sin \left(\pi \cdot \frac{f - Nq}{N} \right) \cdot 2}$$



$$OTF_f := T_f + C_f + S_f \quad OTF_{Nq} := 1$$

$$WRITE(hxxx3) := |OTF_f|$$



Tatian's method of calculating OTF test plot using perfect data

$$Nq = 32 \quad N = 64 \quad n = 0 \dots N - 1$$

$$i = 0 \dots Nq - 1 \quad j = Nq \dots N$$

ideal step

$$Ary_j = 1$$

$$Ary_i = 0$$

$$Ary_{Nq} = .5$$

$$psi_n = \frac{n - Nq}{N} \text{ spatial frequency}$$

$$f = 0 \dots N$$

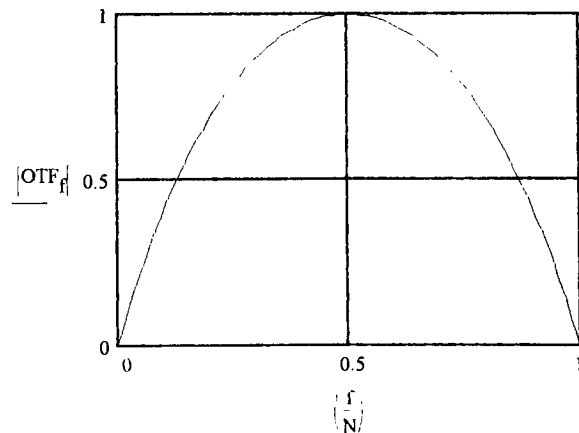
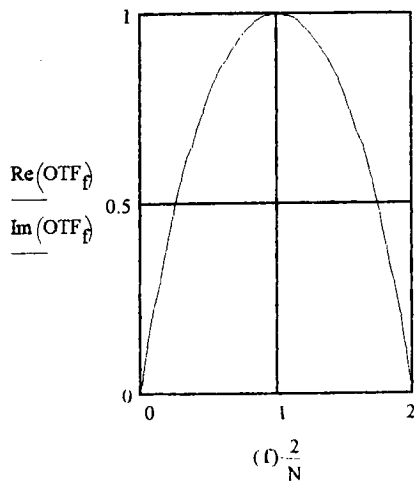
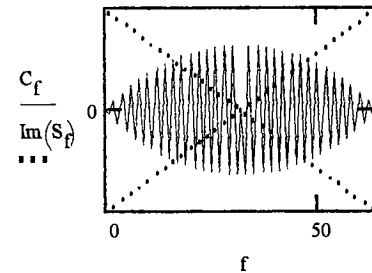
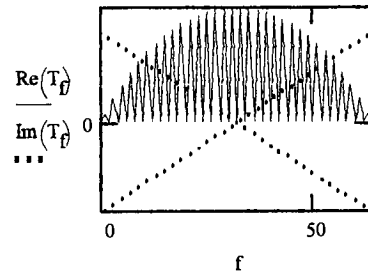
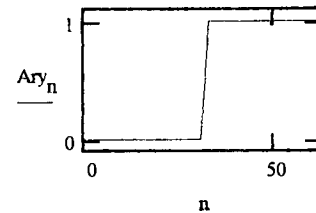
$$T_f = \left[\sum_n \left[Ary_n \cdot \exp \left[-2i \cdot \pi \cdot (f - Nq) \cdot psi_n \right] \right] \right] \cdot 2i \cdot \pi \cdot \frac{(f - Nq)}{N}$$

$$C_f = \frac{\cos \left[(Nq + .5) \cdot 2 \cdot \pi \cdot \frac{(f - Nq)}{N} \right] \cdot 2 \cdot \pi \cdot \frac{(f - Nq)}{N}}{\sin \left[\pi \cdot \frac{(f - Nq)}{N} \right] \cdot 2}$$

$$S_f = \frac{\sin \left[(Nq + .5) \cdot 2 \cdot \pi \cdot \frac{(f - Nq)}{N} \right] \cdot 2i \cdot \pi \cdot \frac{(f - Nq)}{N}}{\sin \left[\pi \cdot \frac{(f - Nq)}{N} \right] \cdot 2}$$

$$OTF_f := T_f + C_f + S_f \quad OTF_{Nq} := 1$$

input data



Tatian's method of calculating OTF test plot using perfect data

$Nq = 32$ $N = 64$ $n = 0 \dots N - 1$

$i = 0 \dots Nq - 1$ $j = Nq \dots N$

ideal step

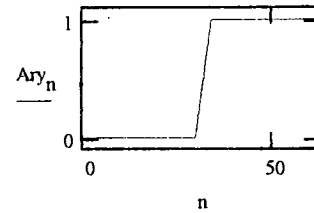
$Ary_j = 1$ $Ary_i = 0$ $Ary_{Nq} = .5$

$Ary_{Nq-1} = .25$ $Ary_{Nq+1} = .75$

$psi_n = \frac{n - Nq}{N}$ spatial frequency

$f = 0 \dots N$

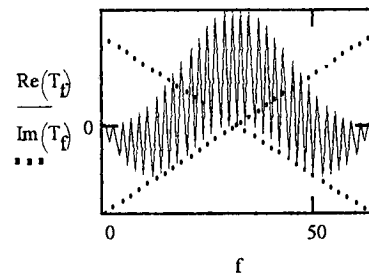
input data



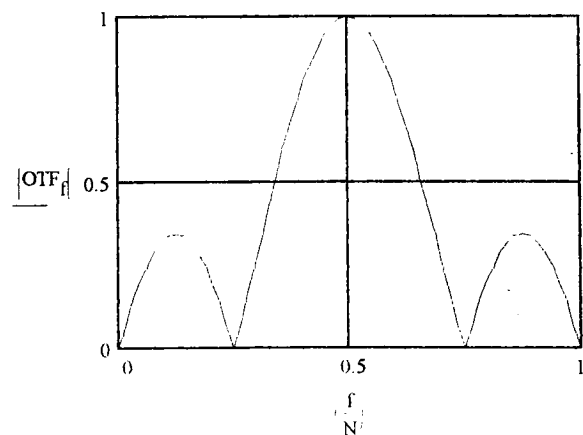
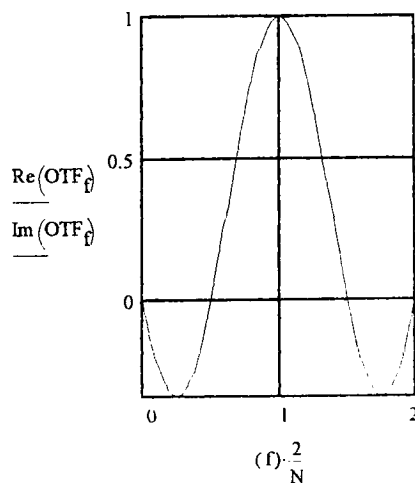
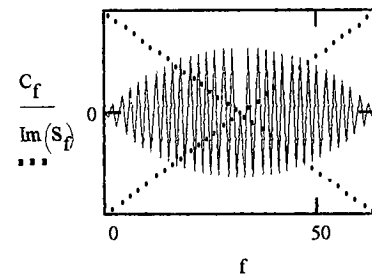
$$T_f := \left[\sum_n \left[Ary_n \cdot \exp \left[-2i \cdot \pi \cdot (f - Nq) \cdot psi_n \right] \right] \right] \cdot 2i \cdot \pi \cdot \frac{(f - Nq)}{N}$$

$$C_f := \frac{\cos \left[(Nq + .5) \cdot 2 \cdot \pi \cdot \frac{(f - Nq)}{N} \right] \cdot 2 \cdot \pi \cdot \frac{(f - Nq)}{N}}{\sin \left[\pi \cdot \frac{(f - Nq)}{N} \right] \cdot 2}$$

$$S_f := \frac{\sin \left[(Nq + .5) \cdot 2 \cdot \pi \cdot \frac{(f - Nq)}{N} \right] \cdot 2i \cdot \pi \cdot \frac{(f - Nq)}{N}}{\sin \left[\pi \cdot \frac{(f - Nq)}{N} \right] \cdot 2}$$



$$OTF_f := T_f + C_f + S_f \quad OTF_{Nq} := 1$$



Tatian's method of calculating OTF test plot using perfect data

$Nq = 32$ $N = 64$ $n = 0 \dots N - 1$

$i = 0 \dots Nq - 1$ $j = Nq \dots N$

ideal step

$Ary_j = 1$ $Ary_i = 0$ $Ary_{Nq} = .5$

$Ary_{Nq-1} = .375$ $Ary_{Nq+1} = .625$ $Ary_{Nq+2} = .75$

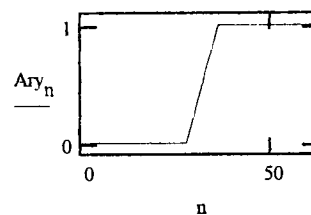
$Ary_{Nq-3} = .125$ $Ary_{Nq+3} = .875$

$Ary_{Nq-2} = .25$

input data

$psi_n = \frac{n - Nq}{N}$ spatial frequency

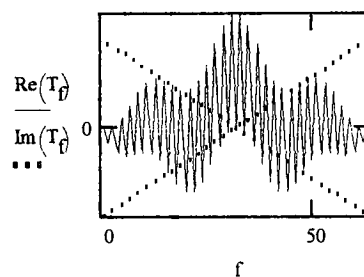
$f = 0 \dots N$



$$T_f = \left[\sum_n \left[Ary_n \cdot \exp \left[-2i \cdot \pi \cdot (f - Nq) \cdot psi_n \right] \right] \right] \cdot 2i \cdot \pi \cdot \frac{(f - Nq)}{N}$$

$$C_f = \frac{\cos \left[(Nq + .5) \cdot 2 \cdot \pi \cdot \frac{(f - Nq)}{N} \right] \cdot 2 \cdot \pi \cdot \frac{(f - Nq)}{N}}{\sin \left[\pi \cdot \frac{(f - Nq)}{N} \right] \cdot 2}$$

$$S_f = \frac{\sin \left[(Nq + .5) \cdot 2 \cdot \pi \cdot \frac{(f - Nq)}{N} \right] \cdot 2i \cdot \pi \cdot \frac{(f - Nq)}{N}}{\sin \left[\pi \cdot \frac{(f - Nq)}{N} \right] \cdot 2}$$



$$OTF_f = T_f + C_f + S_f \quad OTF_{Nq} = 1$$

